# MASTERARBEIT | MASTER'S THESIS

Titel | Title

Detectability of Stellar-Population Dependent Kinematics in Extragalactic Systems Using IFU Spectroscopy

verfasst von | submitted by

Dipl.-Ing. (FH) Margit Schmid BSc

angestrebter akademischer Grad | in partial fulfilment of the requirements for the degree of

Master of Science (MSc)

Wien | Vienna, 2025

| | |
|---|---|
| Studienkennzahl lt. Studienblatt \| Degree programme code as it appears on the student record sheet: | UA 066 861 |
| Studienrichtung lt. Studienblatt \| Degree programme as it appears on the student record sheet: | Masterstudium Astronomie |
| Betreut von \| Supervisor: | Prashin Jethwa MSc MA PhD |

# Acknowledgements

I would like to thank my supervisor, Prashin Jethwa, MSc MA PhD, for his guidance and support throughout this work. I also thank my colleague, Christine Ackerl, BSc MSc, for her assistance and helpful discussions. I am grateful for the input and feedback provided by Univ.-Prof. Dr. Glenn van de Ven and members of his group, as well as for the opportunity to work on this topic.

# Abstract

Understanding galaxy evolution requires accurate measurements of both stellar populations and kinematics, as these properties are tracers of a galaxy's formation history. For instance, observations of the Milky Way show a clear dependence of velocity dispersion on stellar age, illustrating how stellar populations and kinematics are linked. Integral field spectroscopy (IFS) observations performed with integral field units (IFUs) provide collections of 3D spectroscopic data cubes, enabling spatially resolved studies of these properties across different galaxies.

Spectral fitting methods, applied to the resulting IFU data cubes, are commonly used to derive the galaxy properties from observations. A widely used approach is full spectral fitting which typically assumes that all stellar populations at a given location share the same velocity distribution. As a result, spectral fitting methods may miss important physical correlations between stellar populations and kinematics.

In this study, we investigate the feasibility of detecting population-kinematic dependencies with IFU data. We model population-kinematic dependent and independent data cubes from simulation data to quantify the simplification made by fitting methods. We then apply Penalized Pixel-Fitting (pPXF) to the modelled galaxy data cubes and analyze the residuals - the difference between the modelled data cubes and the best fit - across different wavelength regions. Our goal is to investigate whether these residuals reveal measurable information about population-dependent kinematics and assess if they can be used to support observational studies.

Although we obtain residuals of measurable magnitude from the data cubes created with pPXF, our results do not allow us to draw reliable conclusions for the application of our method to real observational data.

# Kurzfassung


Die Erforschung der Galaxienentwicklung erfordert präzise Beobachtungen, sowohl der Sternpopulationen als auch der Kinematik, da diese Eigenschaften wesentliche Hinweise auf die Entstehungsgeschichte einer Galaxie liefern. Studien der Milchstraße zeigen beispielsweise eine deutliche Abhängigkeit der Geschwindigkeitsdispersion vom Alter der Sterne. Dies weist darauf hin, dass Sternpopulationen und Kinematik miteinander verknüpft sind. Beobachtungen mittels Integralfeldspektroskopie (IFS) bzw. Integralfeldeinheiten (engl: integral field units, kurz IFUs), werden als dreidimensionale Spektraldaten (IFU-Data Cubes) bereitgestellt, welche eine räumlich aufgelöste Untersuchung dieser Eigenschaften in unterschiedlichen Galaxien ermöglichen.

Häufig werden spektrale Fitting-Methoden auf diese IFU-Data Cubes angewendet, um die physikalischen Eigenschaften von Galaxien aus den Beobachtungen abzuleiten. Ein gängiger Ansatz dazu ist das Full-Spectral-Fitting, bei dem üblicherweise angenommen wird, dass alle Sternpopulationen an einem gegebenen Ort die gleiche Geschwindigkeitsverteilung besitzen. Infolgedessen können wichtige physikalische Korrelationen zwischen Sternpopulationen und Kinematik unberücksichtigt bleiben.

In dieser Arbeit untersuchen wir die Möglichkeit, Abhängigkeiten zwischen Sternpopulationen und Kinematik mithilfe von IFU-Daten zu erkennen. Wir modellieren sowohl populations-kinematisch abhängige als auch unabhängige Data Cubes auf Grundlage von Simulationsdaten. Dadurch soll untersucht werden, welche Auswirkungen die von der Fitting-Methode verwendete Vereinfachung hat. Anschließend wenden wir Penalized Pixel-Fitting (pPXF) auf die modellierten Data Cubes an und analysieren die Residuen (den Unterschied zwischen den modellierten Data Cubes und dem besten Fit) über verschiedene Wellenlängenbereiche hinweg. Ziel ist es zu prüfen, ob diese Residuen messbare Informationen über Abhängigkeiten zwischen Sternpopulationen und Kinematik beinhalten und ob sie zur Unterstützung von Beobachtungsstudien genutzt werden können.

Obwohl die Residuen der mit pPXF erstellten Data Cubes im messbaren Bereich liegen, ist diese Methode laut unseren Ergebnissen für reale Beobachtungsdaten nicht anwendbar.

# Contents

# List of Tables

# List of Figures

# 1. Introduction

Since it is not possible to observe the full lifecycle of a single galaxy, we rely on reconstructing galaxy evolution by analyzing many galaxies at different evolutionary stages. Stellar populations and kinematics are important properties to help us understand this process. This information can for instance be used to identify merger events in a galaxy's history or to distinguish between scenarios where thick disks are born hot (e.g. Comerón et al. [2019]) or dynamically heated over time (e.g. Yoachim and Dalcanton [2008]).

Conventional fitting techniques applied to observational spectroscopic data use the simplifying assumption that all stellar populations at a given spatial position share the same kinematics, although it is known that old and young stars usually exhibit distinct kinematic behavior. This thesis will investigate how much this assumption affects fitted results by studying the residuals between fitted models and true data. We will also examine how good the quality of the observational data must be to detect any differences.

## 1.1. Galaxy Evolution

A typical galaxy consists of stars, gas, dust and dark matter, distributed among structural components such as the bulge, disk, and halo. Galaxies evolve through a combination of internal processes like star formation, stellar feedback or black hole feedback and external processes like mergers or gas accretion. Observing galaxies at different redshifts, allows us to see them at various stages of their evolution and helps us to reconstruct how galaxies form and change over time.

While we can only observe a galaxy's structure, dynamics and stellar content at one point in time, we can attempt to derive its formation history from these properties. Two very important observational tracers of this history are stellar populations and stellar kinematics. While the distribtion of stellar ages and metallicities can provide information about a galaxy's star formation history and chemical enrichment process, the kinematics, especially the velocity dispersion of stars and rotation curves, indicate how the mass is distributed and how stars have been dynamically heated over time. [Mo et al., 2010]

In disk galaxies, the disk component is often divided into a thick disk and a thin disk, while the central bulge is typically spherical. The thin disk contains most of the gas and young stars and typically represents the component where spiral arms are visible, whereas the thick disk and bulge contain older stellar populations with higher velocity dispersion.

Observations of the Milky Way show that older stars tend to exhibit higher velocity dispersions than younger stars. This indicates the dynamical heating of stars over time and also the conditions under which stars originally formed. For example, thick disk stars are typically older and kinematically hotter than the younger, colder stars of the thin disk. (e.g. Soubiran, C. et al. [2008], Sharma et al. [2021])

In elliptical galaxies and bulges, old stellar populations dominate and show high dispersions due to the pressure-supported nature of these components. [Mo et al., 2010]

## 1.2. Stellar Kinematics

Stellar kinematics refers to the study of the motions of stars within galaxies. These motions are characterized by velocities and velocity dispersions and are key to analyzing a galaxy's mass distribution, formation history, and dynamical properties. While gas cools and settles into rotationally-supported structures, stars retain their kinematic features like velocity dispersion and orbits, which makes them tracers of the galaxy's dynamical history.

The line-of-sight velocity (LOSV) of a star contributes to the Doppler shift observed in its spectrum. In galaxies, the integrated light received from each spatial region in an IFU data cube represents a composite of many stars moving at different velocities. By measuring the Doppler broadening and shifts of absorption lines, we can recover the first and second moments of the line-of-sight velocity distributions (LOSVDs): the mean velocity $V$ and the velocity dispersion $\sigma$. These quantities vary spatially across the galaxy and are typically represented as kinematic maps.

A simple Gaussian function can model the LOSVD as a function of the line-of-sight velocity $v$ [Mo et al., 2010]:

$$\mathrm{LOSVD}(v) = \frac{1}{\sigma\sqrt{2\pi}} \exp\left(-\frac{(v-V)^2}{2\sigma^2}\right) \tag{1.1}$$

Galaxies often show deviations from purely Gaussian velocity distributions. To include these asymmetries and deviations, the LOSVD can be expanded using Gauss-Hermite polynomials and moments:

$$\mathrm{LOSVD}(v) = \frac{1}{\sigma\sqrt{2\pi}} \exp\left(-\frac{(v-V)^2}{2\sigma^2}\right) \left[1 + h_3 H_3\left(\frac{v-V}{\sigma}\right) + h_4 H_4\left(\frac{v-V}{\sigma}\right) + \ldots\right] \tag{1.2}$$

adding $H_j$, the Hermite polynomial of degree $j$ and the Gauss-Hermite moments $h_j (j \geq 3)$. These Gauss-Hermite moments are usually small, which means that the LOSVDs are close to a Gaussian distribution. Including the moments $h_3$ and $h_4$ allows us to refine the fit by including asymmetric variation and symmetric variation [van der Marel and Franx, 1993], which can be interpreted as skewness and kurtosis. (e.g. Hinterer et al. [2022])

Different galactic components exhibit distinct kinematic and stellar population signatures. For instance, stars in thin disks tend to be younger and show relatively cold, rotationally-supported kinematics with low velocity dispersion. In contrast, bulge and halo stars are generally older and exhibit hotter, pressure-supported kinematics with high velocity dispersion, indicating a more turbulent formation history. The thick disk, often considered an intermediate component, contains stars of intermediate age and displays kinematic properties that lie between those of the thin disk and bulge. These properties can help us to infer the course of development of a galaxy.

## 1.3. IFU Data

Understanding galaxy evolution no longer relies solely on traditional 2D optical imaging. With modern instruments we now have access to 3D spectroscopic data cubes, providing spatial as well as spectral information.

Using integral field spectroscopy (IFS), we can dissect a frame into multiple spatial components and obtain a full spectrum at each location. [Bacon et al., 1995] Integral field units (IFUs) are instruments which are able to combine imaging and spectroscopy of each spaxel into one exposure, by dispersing the light of each spaxel.

Important examples of IFU surveys include:

- CALIFA (Calar Alto Legacy Integral Field Area Survey): A survey of 600 galaxies in the local Universe, which represent the sample that can be observed in most detail. [Sánchez et al., 2012]
- Fornax3D: A survey of 33 galaxies associated with the Fornax cluster using the MUSE (Multi Unit Spectroscopic Explorer) IFS at the ESO VLT to study the evolution of galaxies in a dense environment. [Sarzi et al., 2022]
- GECKOS (Generalising Edge-on galaxies and their Chemical bimodalities, Kinematics, and Outflows out to Solar environments): A VLT survey of 35 edge-on disk galaxies with the MUSE IFS to compare galaxies with and without a bar. [van de Sande et al., 2023]
- MaNGA (Mapping Nearby Galaxies at Apache Point Observatory): A survey within the Sloan Digital Sky Survey (SDSS) IV, which observed over 10,000 galaxies with spatially resolved spectroscopy focusing on the study of the kinematic structure and the composition of gas and stars. [Bundy et al., 2015]
- MUSE (Multi Unit Spectroscopic Explorer) Hubble Ultra Deep Survey: Covering 90 % of the Hubble Ultra Deep Field (HUDF), this survey was performed to extend the spectroscopic data library for the objects in this region. [Bacon et al., 2017]

- PINGS (PPAK IFS Nearby Galaxies Survey): A survey of 17 nearby disk galaxies, aiming to obtain continuous coverage spectra across whole galaxy surfaces through spectroscopic mosaicking. [Rosales-Ortega et al., 2010]
- SAMI (Sydney-AAO Multi-object IFS) Galaxy Survey: A survey on the Anglo-Australian Telescope targeting over 3000 galaxies with the main goal to study galaxy evolution in different environements and also the relation between increase of stellar mass and angular momentum. [Allen et al., 2015]
- SAURON (Spectroscopic Areal Unit for Research on Optical Nebulae): A pioneering survey on the William Herschel Telescope (WHT) to study elliptical galaxies and bulges in a sample of over 300 galaxies. [de Zeeuw et al., 2002]

The IFU data cubes resulting from these surveys enable detailed studies of galaxies like analysis of composition, internal structures, dynamics and merger histories to provide new insights about galaxy formation and evolution. (e.g. Sánchez et al. [2012])

However, to derive physical properties such as stellar age, metallicity and kinematics, data modeling and spectral fitting methods are required. Each spectrum in the IFU cube can be a superposition of light from stars with different ages and kinematics, which is a challenge for the tools used to interpret the data.

## 1.4. SSPs

Single stellar populations (SSPs) are populations of stars which are born at the same time and formed from the same initial chemical composition. SSPs are idealized representations of stellar systems like star clusters, which consist of stars with similar ages and chemical composition. We can construct SSP models to characterize unresolved stellar populations in extragalactic galaxies by combining the key components: isochrones, stellar libraries, and the initial mass function (IMF).

Isochrones are the lines on an Hertzsprung-Russell or a Color-Magnitude diagram which connect stars with different masses but with the same age and metallicity. An isochrone depicts what a stellar population would look like at a given age. In an SSP model we can use isochrones to monitor the evolution of stellar populations. Important examples of isochrones include Dartmouth [Dotter et al., 2008] and PARSEC [Bressan et al., 2012].

Stellar libraries provide a collection of theoretical (synthetic) or empirical (observed) stellar properties for different types of stars. These properties can for instance be in the form of full spectra, spectral indices or luminosities. The MILES library, for example, is a library of empirical spectra obtained at the 2.5 m Isaac Newton Telescope (INT). This library provides spectra for 985 stars with a variety of properties in a wavelength range between 3525 and 7500 Å. [Sanchez-Blazquez et al., 2006]

The initial mass function (IMF) defines the distribution of masses in a given stellar population at the time of star formation. This distribution heavily affects how a population evolves, since the properties of stars are closely related to their masses. Examples of widely used IMF forms include the Salpeter [1955], Kroupa [2001] and Chabrier [2003] IMFs.

In its simplest form, a simple stellar population (SSP) is characterized by the spectral energy distribution (SED) of a galaxy as a function of wavelength and time. [van de Ven et al., 2025]

## 1.5. Spectral Modelling

Spectral modelling is used to interpret the information encoded in galaxy spectra and is used to process spectra obtained from IFS. Full spectral fitting methods model an entire observed spectrum unlike methods that only use isolated spectral features.

Usually each spectrum in an IFU cube is a composition of light from stars with different ages, chemical composition and kinematic properties. Using full spectral fitting methods, this information can be extracted from the observed spectra by comparing them to SSP models from libraries. (e.g. Koleva et al. [2009]) A common simplification used in this process is single-component fitting, where it is assumed that all stars contributing to the light in one spatial element share the same kinematics. However, this simplification can overlook important population-specific differences.

Multi-component fitting methods, which allow different stellar populations to have independent kinematics, offer a more realistic picture but also increase model complexity and require higher-quality data to obtain reliable results. There is a variety of tools available to perform such fitting processes, which require the input of appropriate templates and specific configuration parameters.

To better understand the simplifications involved in single-component fitting, we now consider the full stellar distribution function and the assumptions typically made to reduce its complexity.

Following Hinterer et al. [2022], the full distribution function $f(\mathbf{x}, v, z, t)$ for a galaxy describes the probability of finding a star at a specific position $\mathbf{x}$, with a specific velocity (along the line-of-sight) $v$, metallicity $z$ and age $t$. The integral of the stellar distribution function gives the total stellar mass of a galaxy $M^*_{\text{total}}$:

$$M^*_{\text{total}} = \int \int \int \int f(x, v, z, t)\, dx\, dv\, dz\, dt \tag{1.3}$$

The observational data from the IFU is conventionally converted into a 3D data cube $y(\mathbf{x}, \lambda)$. The distribution function $f$ and the data cube $y$ are linked by SSP template spectra $S = S(\lambda; z, t)$.

The relation between $f$, $S$, and $y$ can be written as:

$$\int_{z_{min}}^{z_{max}} \int_{v_{min}}^{v_{max}} \int_{t_{min}}^{t_{max}} \frac{1}{1+v/c} S\left(\frac{\lambda}{1+v/c}; z; t\right) f(\mathbf{x}, v, z, t)\, dt\, dv\, dz = y(\mathbf{x}, \lambda) \tag{1.4}$$

Although the distribution function $f(x, v, z, t)$ is generally a complex function of all four variables, modeling this function is not feasible, because of the high number of correlations between the variables. This is why a single spectrum model makes the assumption that $f$ can be factorized as:

$$f(\mathbf{x}, v, z, t) = f_1(\mathbf{x}) f_2(v|\mathbf{x}) f_3(t, z|\mathbf{x}) \tag{1.5}$$

This factorization splits the distribution function into three independent components. The spatial distribution $f_1(\mathbf{x})$ describes how the stars are distributed across a galaxy. $f_2(v|\mathbf{x})$ describes how the velocities $v$ are distributed at a location $\mathbf{x}$, which corresponds to the line-of-sight velocity distribution (LOSVD). The last term $f_3(t, z|\mathbf{x})$ represents the age and metallicity distribution, i.e. the stellar ages $t$ and metallicities $z$ at a given location $\mathbf{x}$. This formulation assumes that locally, kinematics and populations are independent. [Hinterer et al., 2022]

## 1.6. Summary

As spectroscopic surveys continue to improve in quality and coverage, it is an important task to develop reliable methods to extract the most information from the observed data. To be able to infer galaxy evolution from spectra, it is essential to fit the data with high accuracy.

Given that single-component fitting methods use the assumption 1.5, which does not reflect the complexity of real galaxies, this thesis will quantify the impact of this simplification by comparing original population-kinematic dependent data to constructed population-kinematic independent data cubes. To accomplish this task, we will create data cubes from simulation data to resemble observational data cubes. In the next step we will analyze the residuals resulting from single-component fitting compared to the original data. We will use the spectral fitting software Penalized Pixel-Fitting (`pPXF`) [Cappellari, 2023] to fit our data cubes.

This thesis will also assess the data quality necessary from an observation to be potentially able to detect any residuals and also evaluate which effect the viewing angle has in this context. In addition, the analysis considers the possibility that the residuals themselves may reveil useful information or trends that correlate with different galaxy properties.

# 2. Methodology

In this thesis we want to analyze the impact of the assumption made by full-spectral-fitting methods, that locally, kinematics and populations are independent [Hinterer et al., 2022]. Our approach is to generate different mock IFU cubes from simulation data using the `popkinmocks` [Jethwa, 2023] project. In practice, these data cubes would originate from observations, however, using simulation data allows us to compare our results to the true properties of the galaxies. Using the simulation data, we get a population-kinematic dependent data cube. We will then apply the assumption in Equation 1.5 on one hand, and fit the data using `pPXF` on the other, resulting in two versions of a population-kinematic independent data cube.

After preparing the data cubes, we can calculate the residuals between the different versions. This allows us to estimate the residuals resulting from full spectral fitting and to analyze the differences between all data sets.

## 2.1. Preparation of Simulation Data

This section discusses the selection process of the initial data for this project, as well as how it was obtained and converted to be used with the `popkinmocks` code. We chose to use galaxy data from a cosmological simulation in order to possess all the information regarding the original properties of the galaxies examined in this thesis. This allows us to evaluate the accuracy of the resulting `pPXF` fits.

To obtain the galaxy properties relevant for this project we require a simulation with a sufficiently high resolution. For this project we chose to use data from the IllustrisTNG50 [Pillepich et al., 2019, Nelson et al., 2019] simulation. The TNG50-1 run of the IllustrisTNG project represents the smallest box size and highest resolution run produced in this dark matter simulation project. [Marinacci et al., 2018, Naiman et al., 2018, Nelson et al., 2017, Pillepich et al., 2017a, Springel et al., 2017]

Table 2.1 shows the subset of IllustrisTNG data fields used in this work. The full list of available fields from the IllustrisTNG public data access along with their detailed descriptions can be found on the data specifications page: `https://www.tng-project.org/data/docs/specifications`.

| **Field** | **Dimensions** | **Units** |
|---|---|---|
| Coordinates | N,3 | $ckpc/h$ |
| GFM_Metallicity | N | – |
| GFM_StellarFormationTime | N | – |
| Masses | N | $10^{10} M_{\odot}/h$ |
| Velocities | N,3 | $km\sqrt{a}/s$ |

Table 2.1.: IllustrisTNG data fields used in this work. Each field has a unique name which can be used to filter the downloaded data. The fields are available for $N$ particles and $x$ additional dimensions specific to some of the data fields, in our case 3 (x,y,z) spatial dimensions in their respective units. The metallicity corresponds to the ratio $M_Z/M_{total}$ where $M_Z$ is the total mass of all metal elements (i.e. heavier than He) [I]. The stellar formation time is given as the scalefactor of the exact time when a star was formed [II].

[I] `https://www.tng-project.org/data/docs/specifications/#parttype0`
[II] `https://www.tng-project.org/data/docs/specifications/#parttype4`

### 2.1.1. Choosing a Galaxy Sample

Because galaxy components like bulges and disks have varying kinematic properties and stellar populations with different characteristics, we aim to look at galaxies with differing ratios among their respective components. Pillepich et al. [2024] compiled a subsample of 198 Milky Way and Andromeda analogs at $z = 0$. For this project, we opted to select five galaxies of this subsample, as it includes galaxies of substantial size and with well-resolved structural components.

For all subhalos with at least 10,000 star particles, we can download the supplementary catalog *Galaxy Morphologies (Kinematic) and Bar Properties* [1] from the public data access page. We used the component ratios for the Milky Way and Andromeda analogs from this catalog to choose our subsample of galaxies. Figure 2.1 shows a 3D visualization of the proportions between bulge, thick disk and thin disk of the Pillepich et al. [2024] sample, which we used to decide on the galaxies examined in this thesis. The final selection of galaxies is presented in Table 2.2.

[1] `https://www.tng-project.org/api/TNG50-1/files/morphs_kinematic_bars.hdf5`

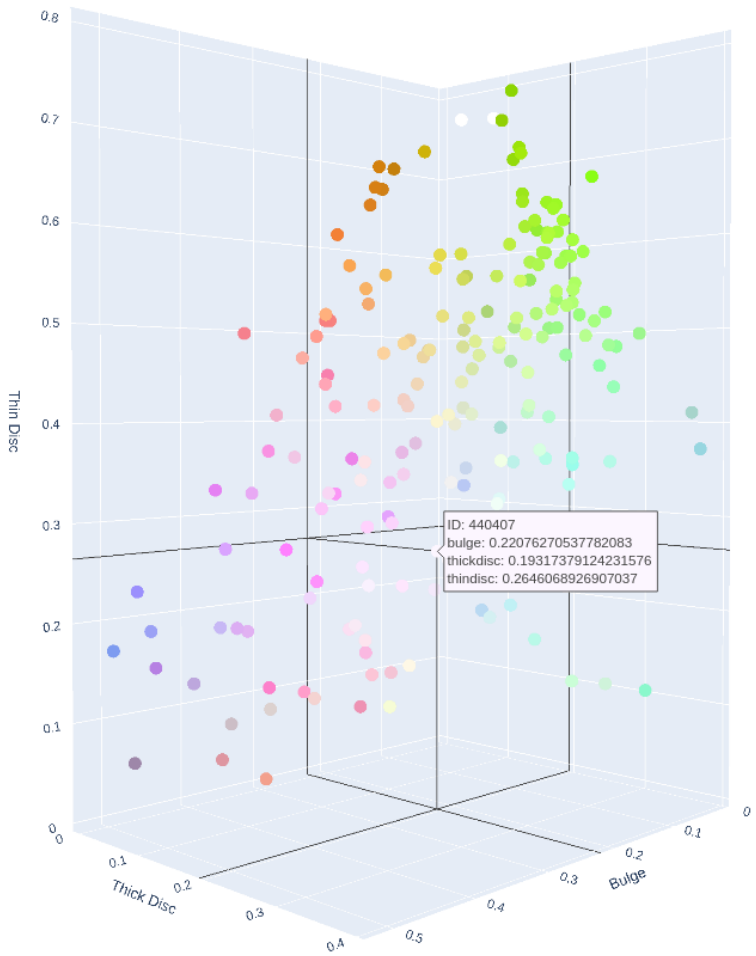


Figure 2.1.: 3D visualization of the TNG50 milky way analog sample from Pillepich et al. [2024] featuring the contributions of bulge, thick disk and thin disk for each galaxy. The colors assigned also represent the proportions of each component through a unique RGB color derived from the respective magnitudes of bulge, thick disk and thin disk to aid in the process of selecting a subsample. The snapshot in this figure shows the process of manually choosing a galaxy sample by considering the location of a galaxy in the 3D space of components.

| **SubhaloID** | **Bulge** | **Thick Disk** | **Thin Disk** | Halo | Pseudo Bulge |
|---|---|---|---|---|---|
| 440407 | 22.08% | 19.32% | 26.46% | 23.38% | 8.76% |
| 469487 | 22.33% | 21.09% | 25.78% | 23.16% | 7.63% |
| 416713 | 47.42% | 0.91% | 5.34% | 35.59% | 10.72% |
| 493433 | 10.97% | 32.91% | 12.78% | 42.52% | 0.83% |
| 342447 | 11.17% | 0.00% | 67.53% | 0.00% | 21.31% |

Table 2.2.: The final galaxy sample used in this thesis, showing the contributions of Bulge, Thick Disk, Thin Disk, Halo, and Pseudo Bulge in percent. Galaxies were selected to include both systems with evenly sized Bulge, Thick Disk, and Thin Disk components, as well as systems in which one component dominates. (All listed components are from the TNG50 *Galaxy Morphologies (Kinematic) and Bar Properties* catalog. The Halo and Pseudo Bulge values are included for completeness but were not used in the selection process.)

### 2.1.2. Downloading and Preparing Galaxy Data

This section will explain the software that was used to download and convert the galaxy data from the IllustrisTNG project and provide the specific methods used for data conversions.

As a base for the data download program we used an existing github repository: `illustrisAPI`[2], which had to be adapted to use the download URLs from the IllustrisTNG project. We retrieved galaxy data for $z = 0$ which corresponds to the TNG50 snapshot 99. The provided code already includes options for unit conversions and the data was converted to the units *kpc*, *Gyr* and $km\,s^{-1}$ during the download.

The metallicity ratio $mr = M_Z/M_{total}$ is not given in solar units. To use the data with `popkinmocks`, we need to convert it to the abundance ratio $M/H$. In the IllustrisTNG data specifications, the primordial solar metallicity is given as $msp = 0.0127$, i.e., the metal mass fraction described in e.g. Wiersma et al. [2009].

The abundance ratio is commonly expressed as

$$\left[\frac{M}{H}\right] = \log_{10}(mr) - \log_{10}(msp) \tag{2.1}$$

with the approximation $M_{\text{total}} \approx M_{\text{H}}$ we use this formula to calculate $M/H$.

[2]`https://github.com/zpenoyre/illustrisAPI.git`.

IllustrisTNG does not provide stellar ages but the stellar formation time in the simulation as the cosmological scalefactor $a$. To calculate stellar ages from the scalefactor we used the `astropy.cosmology` package from the Astropy project [Astropy Collaboration et al., 2013, 2018, 2022]. The `astropy.cosmology` package offers different built-in cosomologies to base calculations on. These cosmologies define for instance the Hubble Constant at a given redshift and assume a flat $\Lambda CDM$ cosmology. For this work we use the Planck15 [Ade et al., 2016] cosmology which was also applied in the IllustrisTNG simulation [Weinberger et al., 2016, Pillepich et al., 2017b]. From the scalefactor $a(t) = 1/(1+z)$ we can derive the redshift $z = (1/a) - 1$ and calculate the age of the universe at that redshift using Astropy. We get the stellar age $t_s$ by subtracting the age of the universe at the stellar formation time $t_z$ from the age of the universe today $t_0$ ($t_s = t_0 - t_z$).

Since this project will examine kinematic properties of galaxies and to make our results comparable and interpretable we want to look at the selected galaxies at specific angles (face-on, 45 deg and edge-on). If we want to create data cubes with `popkinmocks` to look at a galaxy in a specific angle we have to provide the velocity and the coordinates already rotated to this angle. To rotate the prepared galaxy data we used the github repository `rotate_halo` [3], which provides methods to rotate 3D arrays of coordinate and velocity data to desired angles.

At this stage the data is prepared to be used with the `popkinmocks` code. The next section will show how we used the `popkinmocks` project to produce population-kinematic dependent and population-kinematic independent IFU cubes.

## 2.2. Creating IFU Cubes

In this section we will take a look at creating artificial IFU cubes with different characteristics. We will begin by creating a data cube that resembles an observation we would get from an IFU. Still our idealized mock data cube differs from a real observation which would contain inaccuracies due to the instrument and the environmental conditions. The limitations of the resulting data will be discussed in chapter 4.6.

To create a data cube, we need to take the 3D coordinates from the simulated galaxy's stellar particles along with the information for each data point and convert this data into a 2D grid with a full spectrum for each point. From now on we will refer to the spatial components of the cube (i.e. the points in the grid) as spaxels and to each data point in the spectrum as pixel. To convert the simulation data into a data cube we will use the `popkinmocks` project.

[3] `https://github.com/Chia-vie/rotate_halo.git`

`popkinmocks` is a toolset for creating models of galaxy stellar content and generating mock IFU data cubes. It models distributions over stellar population and kinematic parameters using either simulation particle data or a library of parametric galactic components. `popkinmocks` evaluates the stellar integrated-light contribution to the IFU data cube and calculates derived properties like mass or light-weighted moments and probability functions. `popkinmocks` characterizes the stellar content of galaxies through a joint probability distribution over age $t$, line-of-sight (LOS) velocity $v$, 2D on-sky position $\mathbf{x}$ and metallicity $z$. This distribution $p(t, v, \mathbf{x}, z)$ provides a comprehensive description of the relations between stellar population parameters and kinematic variables. The spectra of simple stellar populations (SSPs) are derived from the MILES library (see chapter 1.4). [Jethwa, 2023]

Table 2.3 shows the parameters we have to provide for `popkinmocks`. With those parameters we define the limits of our SSPs templates and the dimensions of our data cube. By restricting the coordinate range we create a cube for the inner 20 kpc of the galaxy.

| **Parameter** | **Value** | **Description** |
|---|---|---|
| `thin_age` | 6 | SSPs stellar age discretisation |
| `thin_z` | 2 | SSPs metallicity discretisation |
| `nx1` | 51 | number of spaxels on the x1 axis |
| `nx2` | 51 | number of spaxels on the x2 axis |
| `nv` | 25 | number of velocity bins |
| `x1rng` | [-20,20] | range of x1 coordinates |
| `x2rng` | [-20,20] | range of x2 coordinates |
| `vrng` | [-1000,1000] | range of v |

Table 2.3.: `popkinmocks` parameters: The parameters `thin_age` and `thin_z` reduce the number of ages and metallicities of our SSPs templates. E.g. setting `thin_z` to 2 results in half the templates regarding metallicities. By setting `nx1` and `nx2` we create a 51 by 51 grid. The spaxels of this grid contain the data of the datapoints which fall in the coordinate ranges `x1rng` and `x2rng` as well as in the velocity range `vrng`. The parameter `nv` defines the number of velocity bins.

Additionally we can now use the data we prepared earlier as input for the data cube. We provide the stellar age, the LOS velocity (corresponding to the $z$-component of the velocity data), the $x$ and $y$ coordinates and the abundance ratio $M/H$ to construct a model from particles. As a first example we use the input data at a 90 degree angle (i.e. edge on) for our sample galaxy 440407 and let `popkinmocks` evaluate Equation 1.4 for our input. In Figure 2.2, we see examples of different plots that can be created from the resulting model, such as a full integrated spectrum and maps of selected properties.

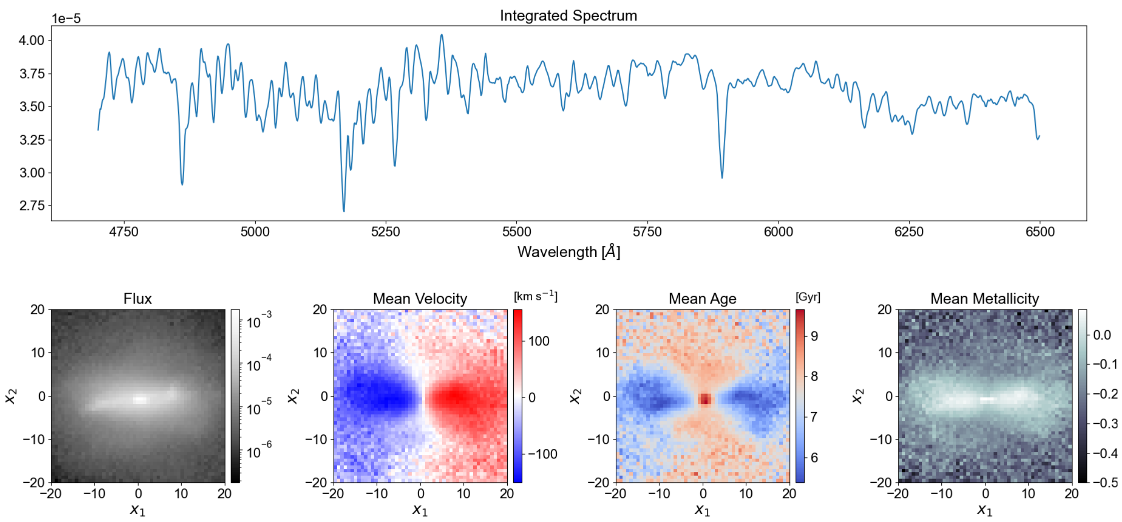


Figure 2.2.: Example plots for the IFU cube created with `popkinmocks` for the TNG50 SubhaloID 440407 edge-on. The top row shows the full integrated spectrum. The bottom row shows 2D visualizations of the flux, the mean velocity, the mean age and the mean metallicity.

The data cube we created represents a joint distribution $p(t, v, \mathbf{x}, z)$ of our simulation data, which means that there is a correlation between kinematics and populations. We refer to this dataset as the *truth*, since it contains the true population-kinematic (PK) correlations. For comparison, we will then create another version of the data cube in which we artificially remove all correlations between stellar populations and kinematics. We refer to this as the PK-independent data cube.

For the PK-independent cube we adopt the simplification from Equation 1.5, which in our case gives us the factorization:

$$p(t, v, \mathbf{x}, z) = p(\mathbf{x})p(v|\mathbf{x})p(t, z|\mathbf{x}) \tag{2.2}$$

which enforces that locally kinematics and populations are independent. We can achieve this by extracting the factors of Equation 2.2 from our PK-dependent cube individually and multiplying them together again. `popkinmocks` provides methods to evaluate probability functions, so as a first step we evaluate $p(\mathbf{x})$, $p(v|\mathbf{x})$ and $p(t, z|\mathbf{x})$ separately. Next we take the products of the probabilities and arrange the dimensions so that they conform to the structure of a data cube created by `popkinmocks`. At last we let `popkinmocks` evaluate Equation 1.4 for the new model.

For a better understanding Figure 2.3 illustrates a simplified version of the process of removing a correlation from a distribution. The process starts with an artificial joint distribution $p(x, y)$. We then extract the probability functions $p(x)$ and $p(y)$. By taking the product $p(x)p(y)$, we assume independence and lose any correlation information.

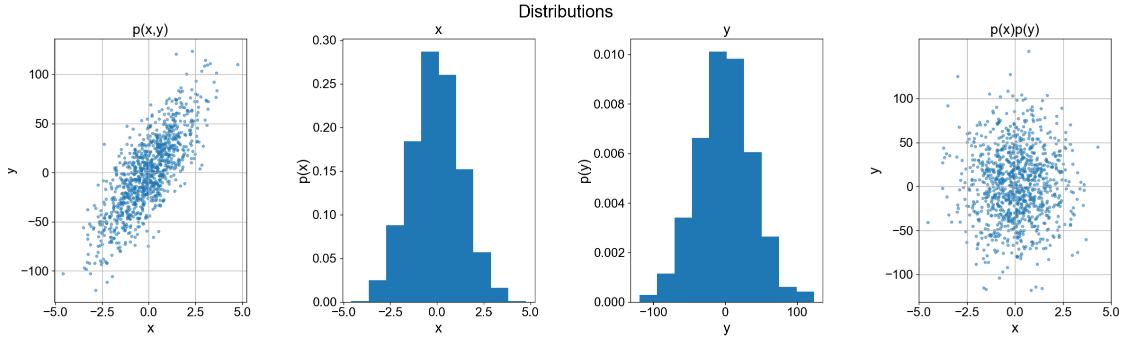


Figure 2.3.: Illustration of creating uncorrelated data: We begin with a joint distribution $p(x, y)$ (left). We then extract the marginal distributions $p(x)$ and $p(y)$ separately (middle). After multiplying the two distributions, we get $p(x)p(y)$ (right) which corresponds to a distribution with no correlation of $x$ and $y$.

Following this process, we created a PK-dependent and a PK-independent version of our model. In the following steps we will compare the properties between the two versions. We start by looking at the full integrated spectra of our galaxy models in Figure 2.4. In the upper panel we can hardly see a difference between the two spectra, in the lower panel we see the calculated difference in percent.

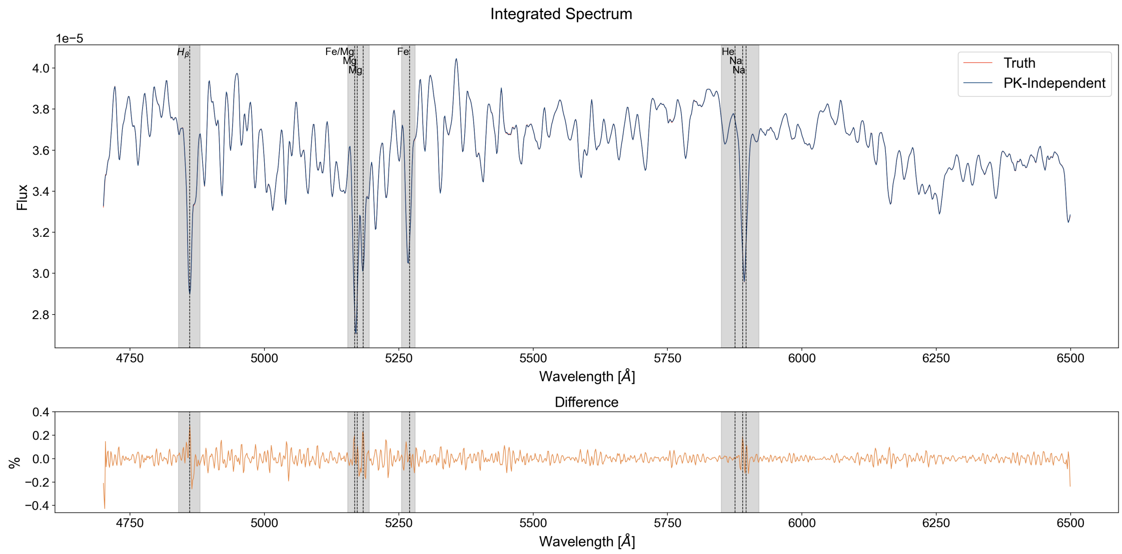


Figure 2.4.: Integrated spectra at a 90-degree (edge-on) angle of the truth and the PK-independent data cube (upper panel) and the difference between the two in percent (lower panel). This difference is very small and the spectra in the upper panel are almost indistinguishable by eye. To investigate in more detail, we mark the strongest lines and select intervals around them (grey boxes).

Since we are looking at the full integrated spectrum in Figure 2.4, we cannot see a significant difference between the two data cubes. We can get into more detail by looking at the most pronounced absorption lines and at the individual spaxels. To do this we choose intervals around the deepest lines including some continuum, as indicated by the grey boxes in Figure 2.4. The intervals are chosen by eye. In Figure 2.5, we show two examples of the spectra around the $H_\beta$ line at the positions $[-11, 0]$ and $[11, 0]$. We can now clearly see a difference between the spectra of the two data cubes.

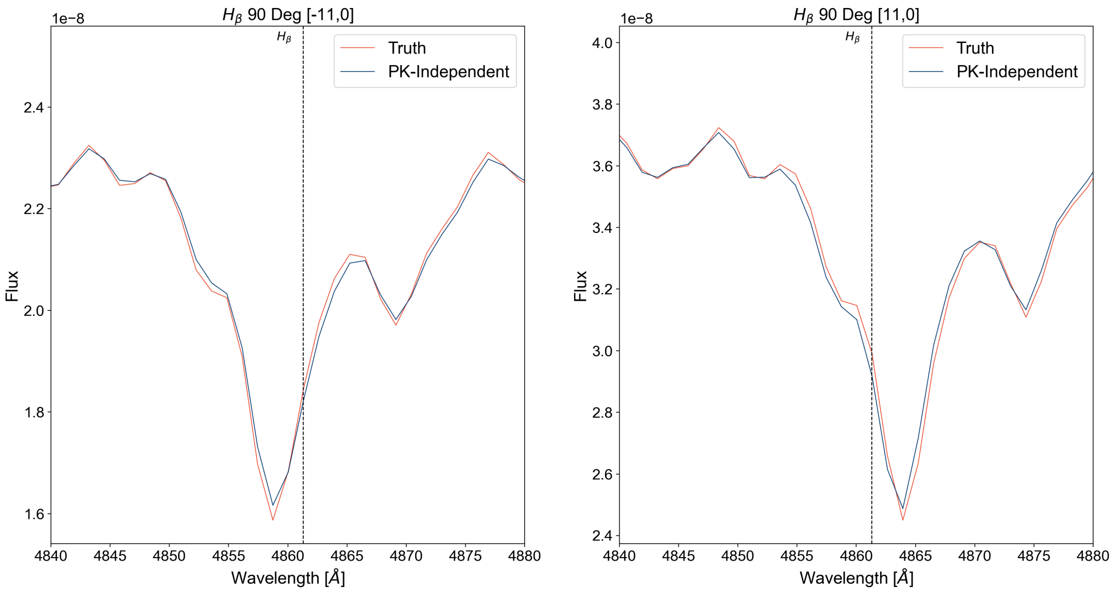


Figure 2.5.: Zoom into the spectra in the interval around $H_\beta$ at two positions $[-11, 0]$ and $[11, 0]$. The galaxy data is again at a 90 degree angle. The spectra of the two data cubes are now clearly distinguishable.

To illustrate this differences for all spaxels we will use difference maps. This implies that for each spaxel we have to calculate one representative value which contains the information of the difference between two spectra. Each of the spectra consists of many data points which are red or blue shifted respective to each other. The next section will describe the metrics we defined to visualize the properties of the differences.

## 2.3. Defining Metrics

As a first step we set some requirements for the metrics we want to use for the difference maps. The values should be easy to calculate and the calculation should not be computationally intensive. Since the difference between two spectra represents a redshift or blueshift, we define that the metrics should indicate the redshift and blueshift respective to the truth.

We define three independent metrics which represent the difference between a truth cube $y_T(\mathbf{x}, \lambda)$ and a PK-independent cube $y_I(\mathbf{x}, \lambda)$ which will be described in the following sections. Each metric is calculated per spaxel, expressed in percent relative to the reference data cube, for every interval we chose in Figure 2.4.

### 2.3.1. Absolute Difference (AD)

The first metric we want to apply is the Absolute Difference (AD) which simply means that we take the absolute value of the difference for each value of $\lambda$ and calculate the mean.

$$AD\left(\mathbf{x}, y_T, y_I\right) = \frac{1}{n_\lambda} \sum_\lambda \left( \frac{|y_T(\mathbf{x}, \lambda) - y_I(\mathbf{x}, \lambda)|}{y_T(\mathbf{x}, \lambda)} \times 100 \right) \tag{2.3}$$

where $n_\lambda$ is the number of flux values in the wavelength range. We multiply the difference by 100 to put it in units of percent. In Figure 2.6 we plot the AD at 0 (face-on), 45 and 90 degrees (edge-on) for the four chosen wavelength intervals. The highest AD values are visible in the interval around the $H_\beta$ line.

In Figure 2.6 we can clearly see a difference between the two data cubes but we can not distinguish if the shift between the spectra is positive or negative. In the next metric we will consider the sign of the shift.

### 2.3.2. Signed Difference (SD)

To distinguish between redshift and blueshift we determine the minimum flux value of the truth spectrum at $\lambda_{min}$. Every difference value up to and including the index of $\lambda_{min}$ we multiply by $(-1)$. We take the mean of the difference values up to $\lambda_{min}$ and add the mean of the difference values after $\lambda_{min}$.

$$\begin{aligned} SD\left(\mathbf{x}, y_T, y_I\right) = &\left( -\frac{1}{n_{1\lambda}} \sum_\lambda \frac{y_T(\mathbf{x}, \lambda) - y_I(\mathbf{x}, \lambda)}{y_T(\mathbf{x}, \lambda)} \times 100 \right) + \\ &\left( \quad \frac{1}{n_{2\lambda}} \sum_\lambda \frac{y_T(\mathbf{x}, \lambda) - y_I(\mathbf{x}, \lambda)}{y_T(\mathbf{x}, \lambda)} \times 100 \right) \end{aligned} \tag{2.4}$$

with $n_{1\lambda}$, the number of flux values where $\lambda \leq \lambda_{min}$ and $n_{1\lambda}$, the number of flux values where $\lambda > \lambda_{min}$ and $n_{1\lambda}$. The SD shows significant values when calculated for the truth and the PK-independent cube, reaching approximately four percent, which we can see in Figure 2.7. We can also see that the differences are not distinct around the galaxy features in the intervals other than $H_\beta$.

With the signed difference we found a calculation which conserves the information if the PK-independent spectrum is shifted left or right respective to the truth. However it does not take into account that other lines and the continuum around the main absorption

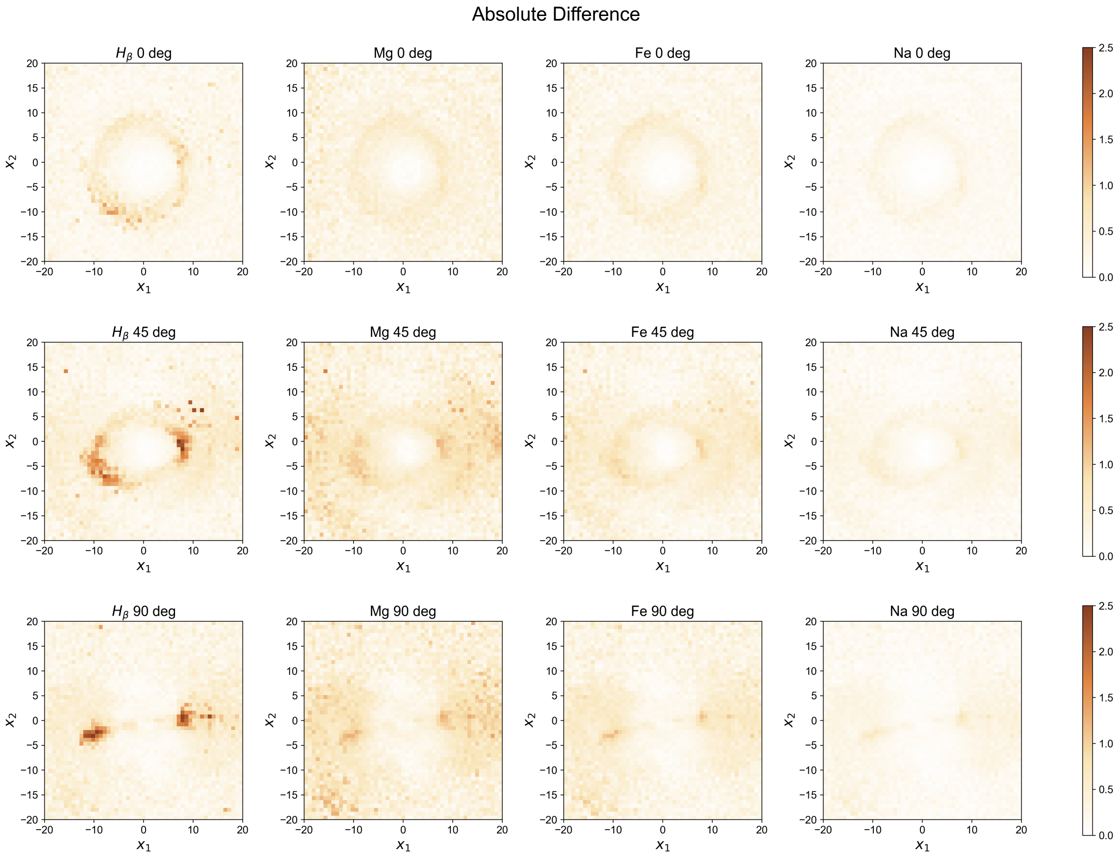


Figure 2.6.: Absolute Difference (AD) at three angles for four different wavelength intervals. The strongest difference can be seen in the $H_\beta$ interval, but all panels show a visible difference at the galaxy features.

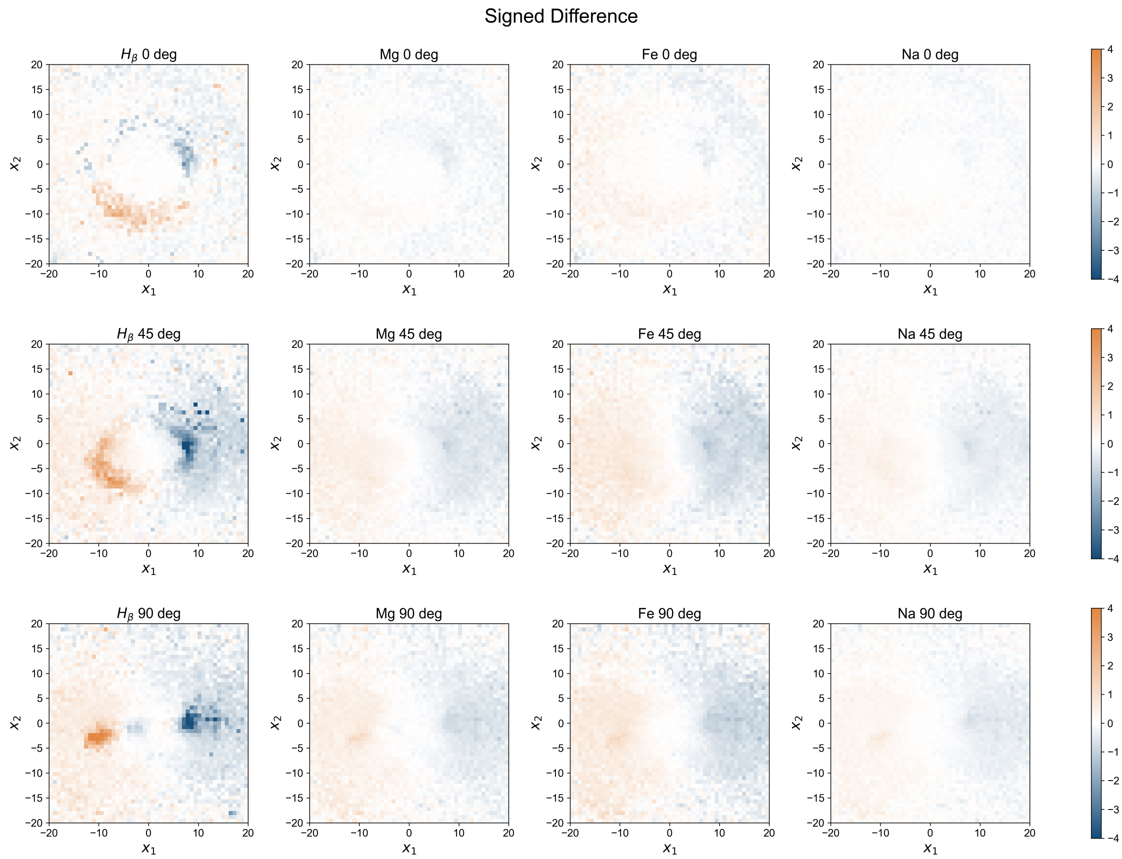


Figure 2.7.: Signed Difference (SD) at three angles for four different wavelength intervals. The strongest difference can again be seen in the $H_\beta$ interval. The other panels also show a difference but the galaxy features are very faint.

line go up and down multiple times before and after the minimum flux value at $\lambda_{min}$. We can see this for instance in the spectra in Figure 2.5 where we see some small lines before and after the main $H_\beta$ absorption line. For the SD all difference values up to $\lambda_{min}$ will be multiplied by $(-1)$ regardless if the slope of the line is going up or down. The next metric will factor in the slope of all lines.

### 2.3.3. Gradient Signed Difference (GSD)

With this metric we want to distinguish between redshift and blueshift and also factor in all the right signs of the differences at every datapoint in the wavelength interval. We calculate the difference for each value of $\lambda$ and weight each value with the sign of the gradient. Then we calculate the mean value.

$$GSD\,(\mathbf{x}, y_T, y_I) = \frac{1}{n_\lambda} \sum_\lambda \frac{y_T(\mathbf{x},\lambda) - y_I(\mathbf{x},\lambda)}{y_T(\mathbf{x},\lambda)} \times 100 \times sgn\left(\frac{dy_T}{d\lambda}\right) \tag{2.5}$$

where $n_\lambda$ is again the number of flux values in the wavelength range and $sgn\left(\frac{dy_T}{d\lambda}\right)$ the sign of the gradient. To estimate the sign of the gradient we look at the flux values. If the flux values decrease, the flux value in the nighbouring wavelength bin is smaller than the one before and vice versa. From this we determine the sign of the gradient and apply it to every value.

In Figure 2.8 we see the difference values with redshift and blueshift. The differences are very distinct around the galaxy features but overall the magnitudes of the GSD values are significantly smaller than of the SD values.

We defined three metrics which each have different qualities but all of them show a significant difference between the truth and the PK-independent cube. So far the SD shows the highest values while also distinguishing between redshift and blueshift. In the next section we will test the qualities of our three metrics and choose the one that is most applicable for this project.

### 2.3.4. Choosing a Metric

At the end of this section we aim to choose the metric that is best suited to highlight the differences between the truth and the PK-independent cube. The SD and GSD can both distinguish between redshift and blueshift, but the SD produces higher difference values than the more accurate GSD. To further investigate the two metrics, we first take a look at the age-velocity distribution. We plot the age-velocity distribution of the truth and the PK-independent cube in Figure 2.9 for the same two spaxels as in Figure 2.5.

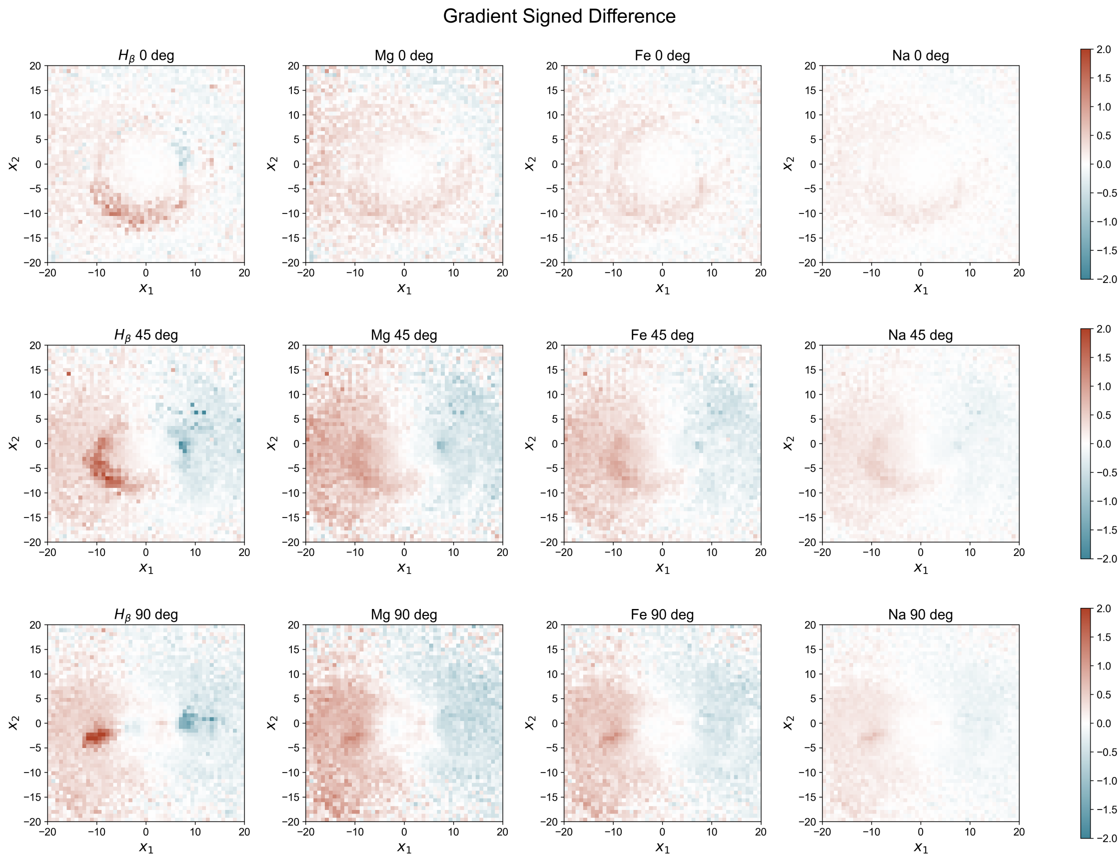


Figure 2.8.: Gradient Signed Difference (GSD) at three angles for four different wavelength intervals. The strongest difference is also in the $H_\beta$ interval and all other panels show a difference at the galaxy features.

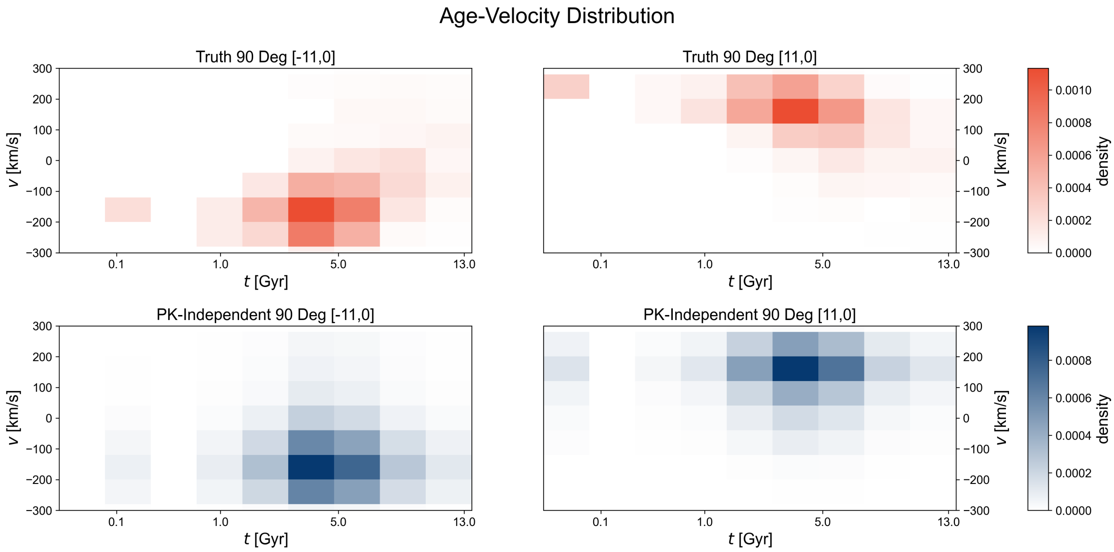


Figure 2.9.: Age-velocity distributions for the truth and PK-independent cube at two positions: $[-11, 0]$ and $[11, 0]$ using the same dataset at a 90 degree angle. We can see that the slope of the distribution is missing for the PK-independent data (lower panels) compared to the truth (upper panels).

From Figure 2.9 we conclude that we can calculate the correlation coefficients of the age-velocity distribution (a-v correlation coefficients) for the truth and use them to check our metrics. We plot each metric against the a-v correlation coefficients in Figure 2.10. We then calculate another correlation coefficient between the values of the metric and the a-v correlation coefficients to test for which metric this correlation is the strongest.

When working with correlation coefficients the values range between $-1$ and 1, where $-1$ corresponds to perfect negative correlation, 0 corresponds to zero correlation and 1 to perfect positive correlation. In the first row of Figure 2.10 we see that for the AD the correlation coefficients are close to 0, which means that there is no significant correlation between the two axes. This is due to the fact that the x-axis data is not in absolute values but the y-axis data which is showing the AD values is in absolute values. We would get higher correlation coefficients if we would use the absolute values of the x-axis data in the calculation, but they would still be significantly lower than the correlation coefficients of the SD and GSD. That is why the AD metric will not be used further in this project.

In Table 3.1 we list the correlation coefficients obtained for all metrics and all angles. As expected the correlation coefficients are higher if the data is at an angle and lower if the data is face-on.

Figure 2.10 and Table 3.1 show that the strongest correlation coefficients can be seen in the SD plots. At higher angles the values get very close to 1, which indicates a very strong correlation. Even though the GSD has a more accurate calculation regarding the slope of the whole continuum, the SD produces the strongest correlation coefficients.

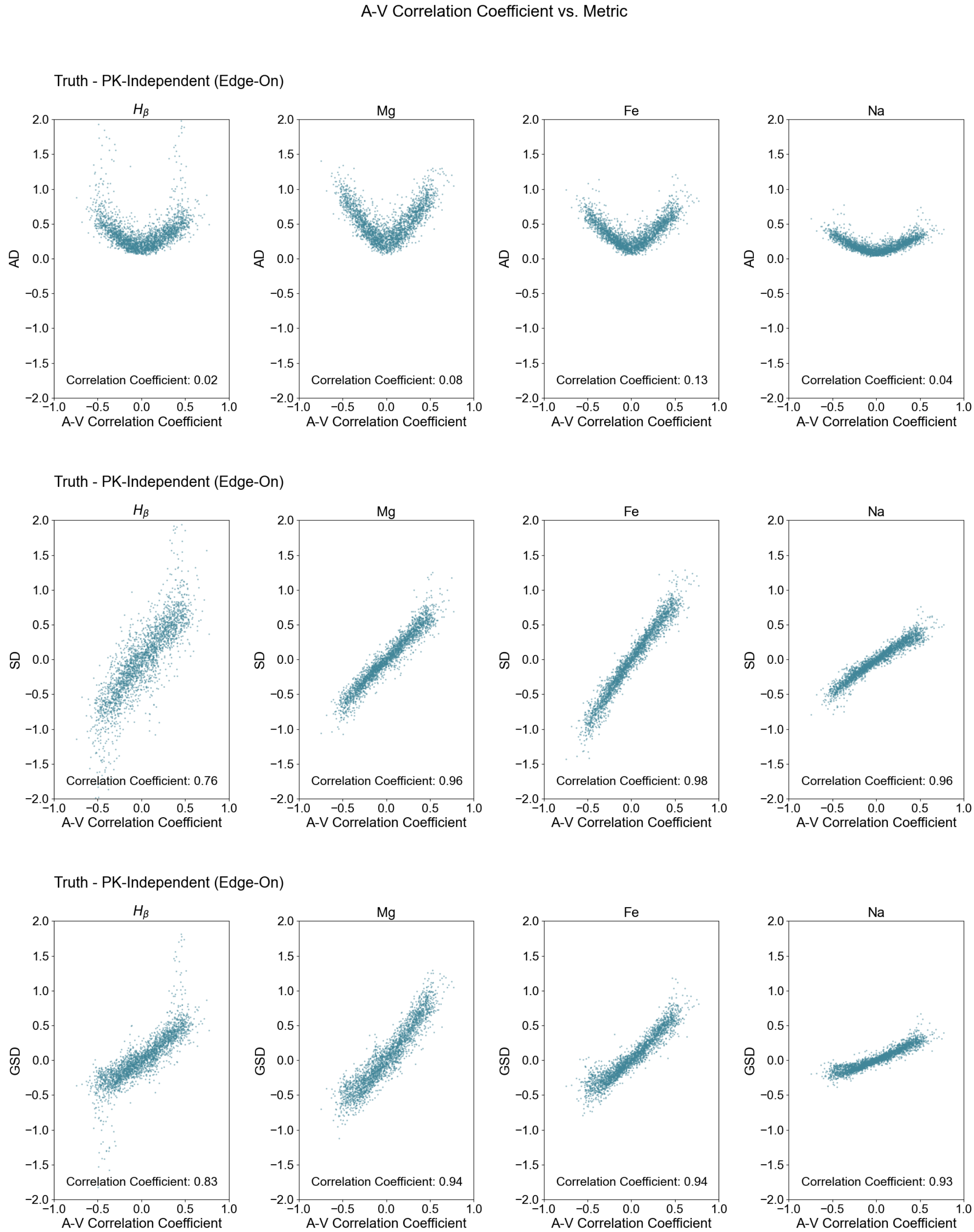


Figure 2.10.: AD, SD and GSD vs. a-v correlation coefficients. We again show the data for the four different wavelength intervals and at a 90 deg angle (edge-on). The correlation coefficients between metric and a-v correlation coefficients can be found in the respective legends. The SD and GSD show very high correlation coeffiecients. The AD does not show any significant correlation coefficients because the age-velocity data is not in absolute values. The highest correlation coefficients are found in the SD panels.

| **Metric** | **Inclination** | $H_\beta$ | $Mg$ | $Fe$ | $Na$ |
|---|---|---|---|---|---|
| AD | face-on | 0.02 | 0.03 | 0.03 | 0.03 |
| | 45 deg | -0.03 | -0.03 | 0.04 | -0.04 |
| | edge-on | 0.02 | 0.08 | 0.13 | 0.04 |
| SD | face-on | 0.39 | 0.83 | 0.87 | 0.84 |
| | 45 deg | 0.73 | 0.96 | 0.96 | 0.95 |
| | edge-on | 0.76 | 0.96 | 0.98 | 0.96 |
| GSD | face-on | 0.50 | 0.74 | 0.76 | 0.72 |
| | 45 deg | 0.79 | 0.92 | 0.92 | 0.90 |
| | edge-on | 0.83 | 0.94 | 0.94 | 0.93 |

Table 2.4.: Correlation coefficients for AD, SD and GSD for all angles and the four different wavelength intervals. The correlation coefficients for the AD are close to 0 at all angles. For the SD and GSD the highest correlation coefficients can be obtained with the edge-on data. Overall the SD shows the highest correlation coefficients.

This is because the SD focuses on the main absorption line, while the GSD includes the slopes of all the lines in the chosen intervals. Since the main absorption line contains the information we want to investigate, the SD will be the primary metric used from here on in this study.

As a last step we want to examine why the strongest differences between the thruth and the PK-independent cube are visible around the $H_\beta$ line. Since Balmer lines, unlike metal lines, are strong in young stars (e.g. González Delgado et al. [1999]) and the strong galaxy features visible in Figure 2.7 appear to correspond to young regions of the galaxy, we want to test if these features are produced by young stars. We generate the same plots as in Figure 2.7, but prior to creating the data cubes, we filter out the data points to retain only those with ages greater than 1.5 Gyr. The results are shown in Figure 2.11. The strong features have completely disappeared and we can conclude that the highest differences between truth and PK-independent cube are indeed caused by young stars.

After creating data cubes from IllustrisTNG simulation data we were able to create PK-independent cubes using the assumption in Formula 1.5. To evaluate the difference between the truth and the PK-independent version of a data cube we defined different metrics. We found a strong correlation between the metrics and the a-v correlation coefficients of the truth. After evaluating all results up to this point, we chose to continue this work with the SD metric because it distinguishes between redshift and blueshift and also emphasizes the main absorption line, which is significant for this project.

So far, we have been working with very idealized simulation data. In the next section, we will apply the same concepts to data that more closely resembles observational data.

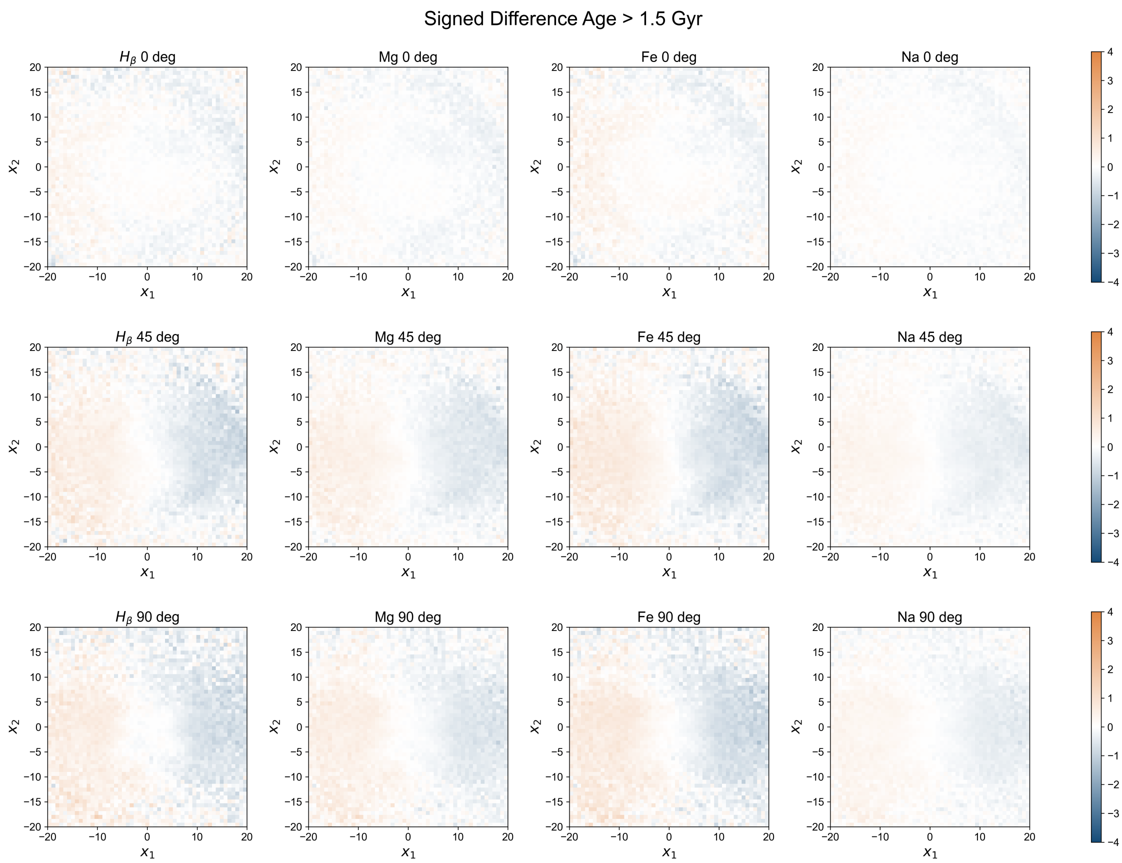


Figure 2.11.: SD for a filtered dataset with ages > 1.5 Gyr at three angles for four different wavelength intervals. The galaxy features visible in the $H_\beta$ panels of Figure 2.7 are absent in this version, which does not include young stars.

We cannot directly observe the contents of a PK-independent cube, but we can fit the spectral components of our truth cube using spectral analysis software, which would also be used to fit observed spectra.

## 2.4. Fitting IFU Cubes

In the previous sections we have successfully generated mock data cubes from IllustrisTNG simulation data and identified metrics to quantify the differences between the truth and the PK-independent cube. Next, we want to determine if the same effects can be observed when using a data cube generated by a spectral analysis code instead of the PK-independent cube.

For this work we are using Penalized pixel-fitting (`pPXF`) Cappellari [2023], which is a commonly used spectral analysis code. Through full spectrum fitting, observed spectra are matched with provided template spectra to infer the kinematics of stars and gas. Cappellari [2017] To create a comparable data cube using `pPXF` we will only provide the spectral component of the truth data cube. For fitting, we use the same MILES templates as were used when the data cube was created with `popkinmocks`.

Since `pPXF` fits spectra using the assumption 1.5, we would expect that our fitted data cube (PPFX fit to truth) has the same properties as the PK-independent cube. After fitting the truth with `pPXF` we will use the SD and correlation coefficients to compare the results.

### 2.4.1. Fitting Data

In this section we will describe our approach to fit the truth cube with `pPXF` and the parameters used to get the best result.

At first we create the truth cube with exactly the same data and parameters as described in section 2.2. From the truth we extract the MILES templates using `popkinmocks`, to provide exactly the same templates to `pPXF`. We use only the spectral component of the data cube for the fitting process.

Since we are working with simulation data, we are able to compare the output of the fitting process with the original data and were able to try different approaches and combinations of parameters to get the best fitting results. We found that changing the resolution of the truth data cube did not have a significant impact on the fit and the overall results. Regarding the `pPXF` parameters, changing the number of moments and the fitting tolerance did not change the results significantly. The two parameters that affected the quality of the fit the most, are the start values for the LOSVD, specifically the velocity $v$ and the velocity dispersion $\sigma$. Varying those parameters lead to significantly different results in the outer region of the galaxy. The central region of the galaxy was not highly sensitive to $v$ and $\sigma$. Since `pPXF` fits each spaxel separately we found that varying $v$ and $\sigma$ for every spaxel gave the best result. We let `pPXF` fit each spaxel with different combinations of starting positions and chose the best fit per spaxel using the return parameter $chi2$.

Table 2.5 shows the parameters used to create the best `pPXF` fit to the truth cube.

| **Parameter** | **Value** | **Dimension** | **Description** |
|---|---|---|---|
| `templates` | | arr(1215, 9, 6) | 3D array of spectral templates: (n_pixels_temp, n_age, n_metal) |
| `galaxy` | | arr(1215) | galaxy(n_pixels,): spectral data of one spaxel |
| `noise` | | arr(1215) | noise(n_pixels,), all pixels set to 1 |
| `velscale` | 80 | | velocity resolution |
| `start` | | arr(1, 1) | start = [velStart, sigmaStart]: start values for $v$ and $\sigma$ |
| `ftol` | 1e-4 | | fitting tolerance |
| `goodpixels` | | arr(1206) | indices of good pixels in spectrum (n_pixels,) |
| `moments` | 4 | | number of Gaussian moments |

Table 2.5.: `pPXF` parameters used with their respective values or dimensions that were used in this work. We provided 3-dimensional `templates` with spectra per age and metallicity. The array `galaxy` contains the spectral data to be fitted, corresponding to one spaxel of the data cube. Since our data does not have any noise, we provide the same value 1 for all pixels to the parameter `noise`. The value of the velocity resolution `velscale` results from the `popkinmocks` parameters `nv` and `vrange` (2000/25 = 80). The array `start` provides the initial guesses for each moment $(v, \sigma, h3, h4, \ldots)$. We provided one of the combinations between $velStart = [-250, -150, 0, 150, 250]$ and $sigmaStart = [70, 125, 180]$ for each run. Moments without provided values are set to 0. `ftol` controls the convergence tolerance for the fitting procedure and is set to a recommended value. With the array `goodpixels` we cut off artifacts in the spectra from `popkinmocks`. We initially chose to model the LOSVD with 4 `moments` $(v, \sigma, h3, h4)$.

In Figure 2.12 we see the resulting integrated spectrum of the `pPXF` fit to truth fitted with the methods and parameters described above, compared to the integrated spectrum of the truth. Similar to Figure 2.4 the two lines are not really distinguishable by eye, which means that our fitting method worked well.

For a detailed comparison, Figure 2.13 again shows the spectra around the $H_\beta$ line at the positions $[-11, 0]$ and $[11, 0]$ (the same positions as in Figure 2.5). This time we compare the `pPXF` fit to truth with the truth and for reference we see the PK-independent spectrum from Figure 2.5 as a dotted line.

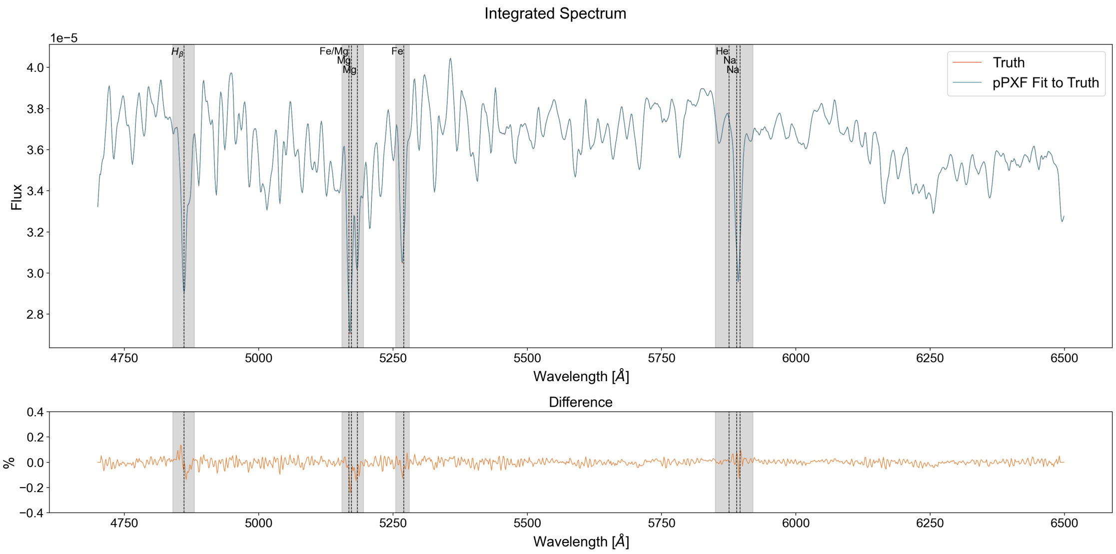


Figure 2.12.: Integrated spectra at a 90 degree (edge-on) angle of the truth and the `pPXF` fit to truth (upper panel); the difference between the two in percent (lower panel). This difference is again very small and the spectra in the upper panel are almost indistinguishable by eye, which means the data was fitted well with `pPXF`.

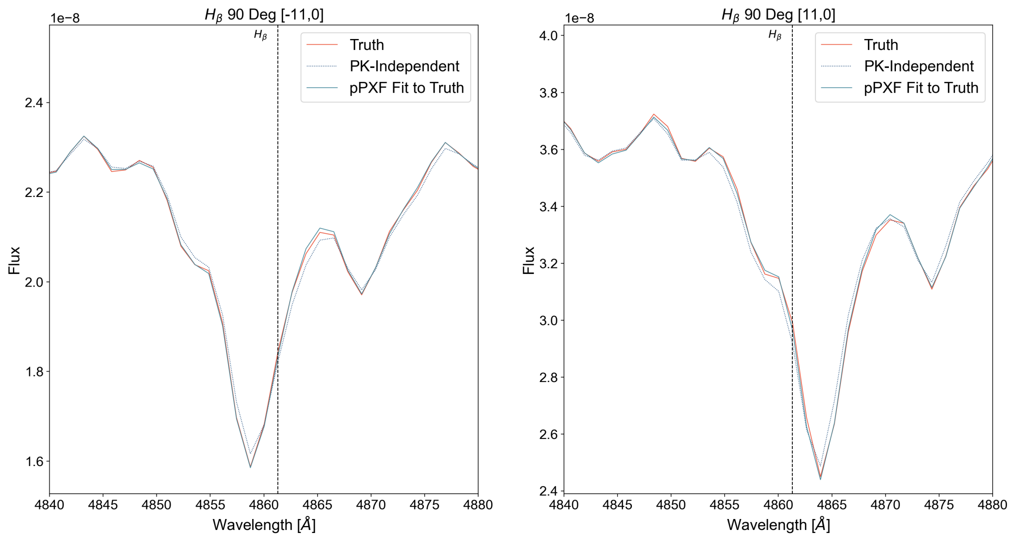


Figure 2.13.: Zoom into the spectra in the interval around $H_\beta$ at two positions $[-11, 0]$ and $[11, 0]$. The galaxy data is at a 90 degree angle. The lines are now distinguishable and we can see the shift between the different spectra.

From the spectra in Figure 2.12 and Figure 2.13 we can infer that our fitting method is working reasonably well and the resulting `pPXF` fit to truth is a close fit.

To further investigate these results, we can take a look specifically at the velocities and $\sigma$ values which were fitted by `pPXF`. We plot the light weighted mean velocities of the truth data cube, the velocity of the `pPXF` fit to truth and their difference in Figure 2.14. We plot the $\sigma$ values respectively.

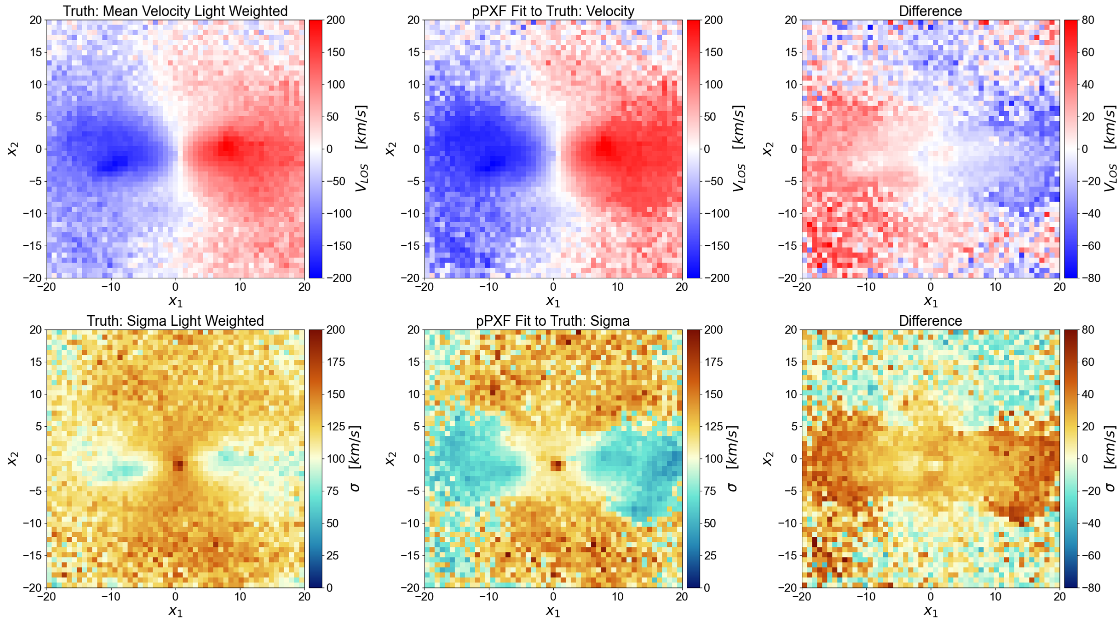


Figure 2.14.: Light weighted velocity and $\sigma$ of truth in the left panels, velocity and $\sigma$ of the `pPXF` fit to truth in the middle panels and the respective differences in the right panels. The residuals in the velocity are close to the velocity resolution of 80.

Figure 2.14 shows differences in the velocity between the truth and the `pPXF` fit to truth, with values being close to the velocity resolution of 80. The velocity amplitudes in the `pPXF` fit seem to be overestimated, while there is a big region in the area of the disk with low sigma compared to the truth.

Even though there are differences in the velocities and $\sigma$, they are consistent with expected level of accuracy. Based on our analysis so far, the spectra of the truth and the `pPXF` fit to the truth are similar enough to assume that the fit is adequate. To double-check this result, we will apply the same `pPXF` fit as described in Table 2.5 to the PK-independent cube.

### 2.4.2. PPXF Fit to PK-Independent

If we apply the same `pPXF` fitting method to the PK-independent cube instead of the truth, we would expect zero residuals since the assumption from Formula 1.5 had already been taken into account in the data. Thus it should not make a difference if `pPXF` applies the same assumption again while fitting the data. We generate the SD for the obtained fits and plot the results in Figure 2.15.

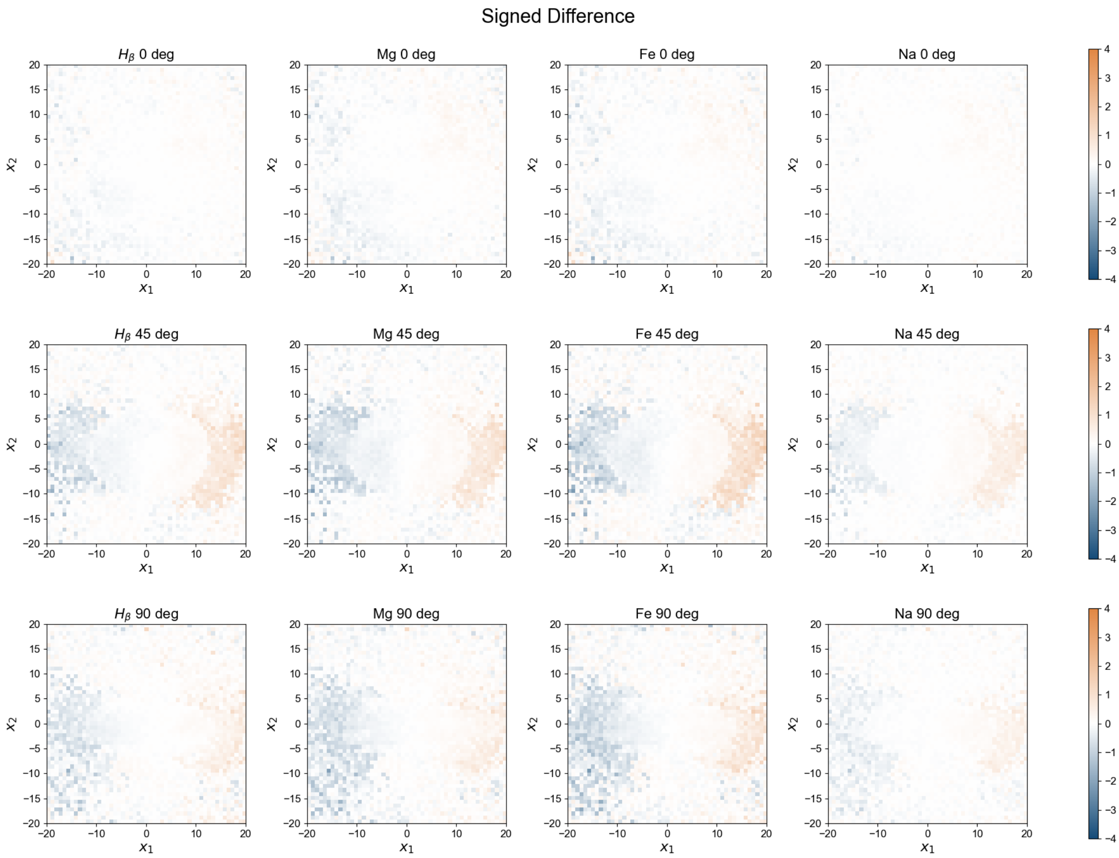


Figure 2.15.: SD for `pPXF` fit to PK-independent and PK-independent at three angles for four different wavelength intervals. The strong features of the galaxy are not visible in this version. There are visible residuals on the outside of the center, which have opposite signs compared to the SD for the PK-independent cube in Figure 2.7.

Figure 2.15, as expected, shows no strong galaxy features and lower SD values compared to Figure 2.7. Outside of the galaxy center, there are some residuals, which show opposite signs compared to the same regions in Figure 2.7 and Figure 2.11. Maybe the applied fourth-order Gauss-Hermite model is not well-suited for these regions.

After analyzing the quality of our fitting method with `pPXF`, we will now apply the SD to the `pPXF` fit to truth to investigate whether we can draw conclusions from the `pPXF` residuals regarding the assumption in Formula 1.5.

# 3. Results

After fitting the true data cube with `pPXF`, we can see that the fitted integrated spectrum is in close agreement with the integrated spectrum of the true data cube. To analyze the fit in more detail, we will examine the residuals by looking at the SD, as well as calculating correlation coefficients and standard deviations. This will allow us to assess whether the residuals reveal any information or contain systematic trends related to the underlying galaxy properties.

## 3.1. Signed Difference SD

In the first step, we will examine the `pPXF` fit based on the parameters described in Table 2.5. In Figure 3.1 we plot the SD for the `pPXF` fit to truth at three angles (face-on, 45 deg and edge-on) and with the intervals we defined in Figure 2.4. The SD at the galaxy features is less significant than in the PK-independent version shown in Figure 2.7, and in the outer parts of the galaxy some signs are switched when comparing the two versions.

We want to investigate which moments are responsible for the different results in the SD when comparing the PK-independent cube created with `popkinmocks` and the `pPXF` fit to truth. To do this, we will fit our data again using different options for the moments parameter.

In `pPXF`, we have the option to either let `pPXF` fit all required Gaussian moments or provide fixed values for certain moments to the function. We execute the `pPXF` fit to truth again but provide the values for $v$ and $\sigma$ (from the truth data cube) for every spaxel. This means that `pPXF` adopts the provided values for $v$ and $\sigma$ and only fits the moments $h3$ and $h4$. We will refer to this version as `pPXF` fixed fit to truth, or `pPXF` fixed fit in short.

In another version of the `pPXF` fit, we exclude $h3$ and $h4$ and only let `pPXF` fit two moments, $v$ and $\sigma$, to see if there is a significant difference between the two fits. We will call this version `pPXF` fit to truth 2 moments or `pPXF` fit 2M for short.

After creating different versions of the `pPXF` fit, we will take a look at the correlation between the SD and the a-v correlation coefficients to investigate if the different options for the moments in the `pPXF` fit have an effect on the correlations.

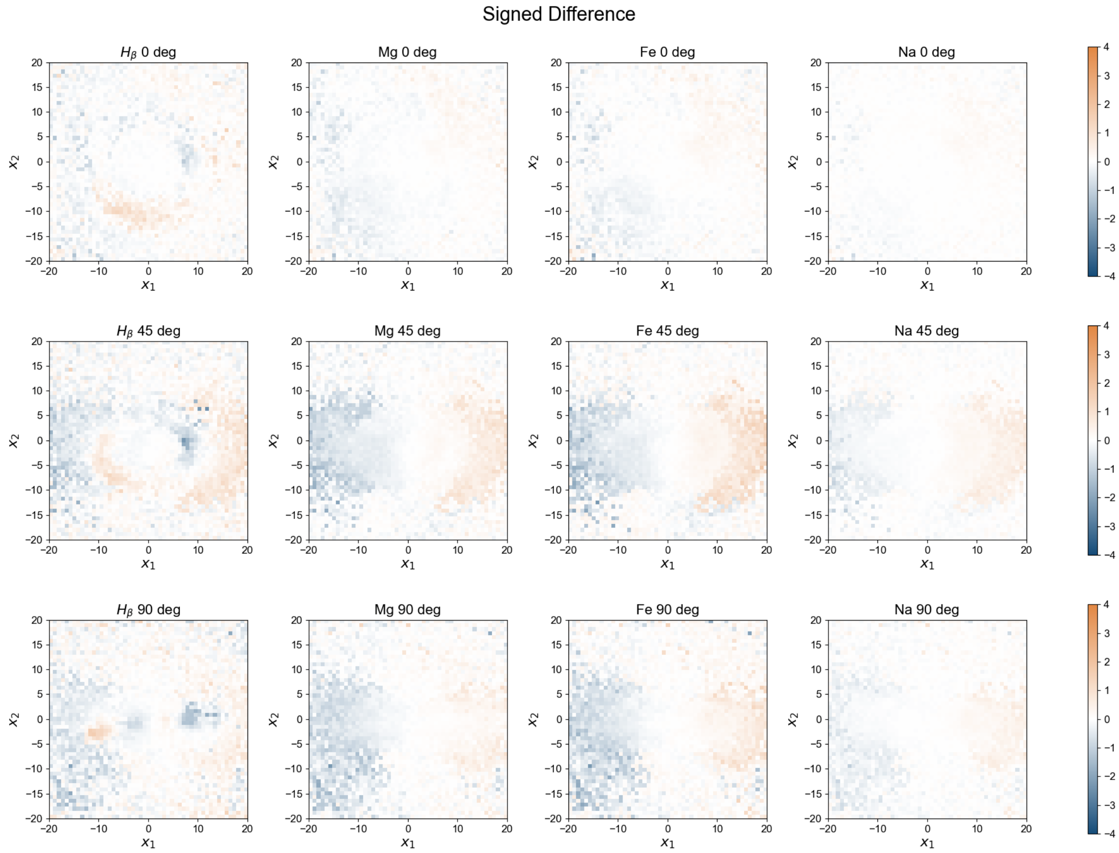


Figure 3.1.: SD for `pPXF` fit to truth at three angles for four different wavelength intervals. We can clearly see the galaxy features in the $H_\beta$ panels. If we compare this result to the SD for the PK-independent cube in Figure 2.7 we see that the features are fainter for the `pPXF` fit to truth. We also see that the sign of the SD in the outer part of the galaxy is switched compared to Figure 2.7.

## 3.2. Correlation Coefficients

In this step we want to compare the correlation coefficients for four different data cube versions. In Figure 3.2 we plot the correlations between the a-v correlation coefficients (x-axes) and the SD (y-axes) around four different absorption features (columns). The top row of Figure 3.2 shows the SD of the truth - PK-independent (i.e. repeating the middle row in Figure 2.10). It represents the strong correlation we would expect between the SD of the truth - a datacube which uses the assumption 1.5 and the a-v correlation coefficients.

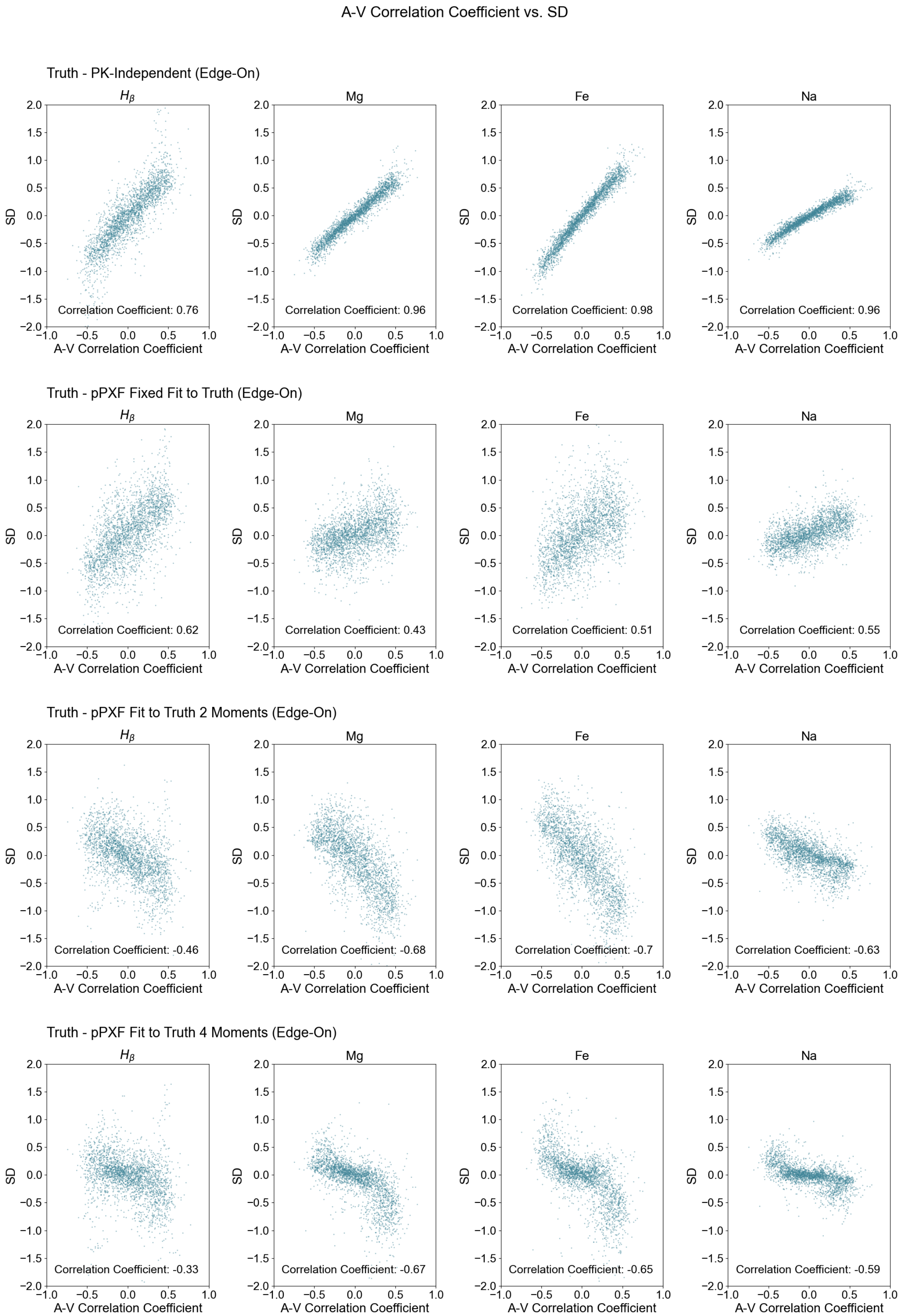


Figure 3.2.: SD vs. a-v correlation coefficients at four different wavelength intervals and at a 90 deg angle (edge-on) for the Kin. Ind. cube and three different fitting combinations with `pPXF`.

Rows 2-4 of 3.2 show the correlations of `pPXF` fit residuals for the different fit configurations described above. The second row shows the correlation coefficients when $v$ and $\sigma$ are fixed. We can see that the same overall trend is present, but the correlation is weaker and the points show noticeably more scatter. Even though `pPXF` fit only the moments $h3$ and $h4$, there is a significant change in the correlation. In the third row we plot the correlation coefficients when `pPXF` fits only $v$ and $\sigma$ ($h3$ and $h4$ are excluded). We see a reversal in the correlation direction, with the coefficients switching from positive to negative while the correlation strength remains similar to the second row. The last row presents the correlation coefficients for the `pPXF` fit of the four Gaussian moments $v$, $\sigma$, $h3$ and $h4$. We can see that the distributions are slightly more distorted compared to the third row, with a small reduction in correlation strength.

We obtain significant correlation coefficients for all versions of the `pPXF` fit, but notably, Figure 3.2 shows that the correlation direction shifts when `pPXF` fits $v$ and $\sigma$.

So far, the results presented correspond to one galaxy in our sample (SubhaloID 440407). Table 3.1 lists the strength of the correlations between the SD of `pPXF` fit residuals and the respective correlation coefficients for the full galaxy subsample. The corresponding correlation coefficient plots for the remaining galaxy sample are presented in Appendix A.1.

| | Truth - PK-Ind. | | | | Truth - `pPXF` Fixed Fit | | | | Truth - `pPXF` Fit 2M | | | | Truth - `pPXF` Fit | | | |
|---|---|---|---|---|---|---|---|---|---|---|---|---|---|---|---|---|
| Subhalo | $H_\beta$ | $Mg$ | $Fe$ | $Na$ | $H_\beta$ | $Mg$ | $Fe$ | $Na$ | $H_\beta$ | $Mg$ | $Fe$ | $Na$ | $H_\beta$ | $Mg$ | $Fe$ | $Na$ |
| 440407 | 0.76 | 0.96 | 0.98 | 0.96 | 0.62 | 0.43 | 0.51 | 0.55 | -0.46 | -0.68 | -0.70 | -0.63 | -0.33 | -0.67 | -0.65 | -0.59 |
| 469487 | 0.40 | 0.84 | 0.88 | 0.87 | 0.05 | 0.10 | 0.20 | 0.21 | -0.26 | -0.16 | -0.12 | -0.09 | -0.26 | -0.18 | -0.15 | -0.11 |
| 416713 | 0.76 | 0.85 | 0.86 | 0.82 | 0.70 | -0.16 | -0.19 | -0.24 | 0.57 | -0.48 | -0.54 | -0.63 | 0.61 | -0.50 | -0.54 | -0.63 |
| 493433 | 0.66 | 0.86 | 0.90 | 0.85 | 0.47 | -0.04 | -0.02 | -0.01 | 0.20 | -0.33 | -0.34 | -0.31 | 0.29 | -0.35 | -0.32 | -0.30 |
| 342447 | 0.37 | 0.77 | 0.80 | 0.75 | 0.23 | 0.26 | 0.33 | 0.36 | -0.32 | -0.43 | -0.43 | -0.38 | -0.25 | -0.38 | -0.37 | -0.33 |

Table 3.1.: Correlation coefficients for the chosen galaxy sample at a 90 deg angle (edge-on). The correlation coefficients are high for the Truth - PK-Ind. version for all galaxies but this does not reflect in the fitted versions.

Based on the first group of columns in Table 3.1, which represents the PK-independent data cube, we would expect similarly high correlation coefficients throughout the whole galaxy sample. However Table 3.1 shows that this is not the case. As `pPXF` is allowed to fit more kinematic moments, the magnitudes of the correlations vary considerably.

Only for galaxy 440407 the sign of the correlation appears to switch between the fit with fixed $v$ and $\sigma$ and the version where `pPXF` fits these moments. Nonetheless, the correlation coefficients vary significantly between the two fitting versions for the remaining galaxy sample.

Galaxy 469487, with an even component distribution comparable to galaxy 440407 shows significantly lower correlation coefficients. The only galaxy that shows a stronger correlation besides 440407 is galaxy 416713 with a dominant bulge component. The galaxies with dominant thick disk and thin disk (493433 and 342447) show moderate magnitudes of correlation coefficients, but none of them is close to the results from the respective PK-independent data cubes.

Since `pPXF` tries to fit the data to the truth as close as possible according to the methods and templates available, this might result in a different outcome of the fitted data compared to the calculated PK-independent data. If we go back to Figure 2.13 we can see that calculating the PK-independent spectra made the lines slightly flatter whereas the `pPXF` fit made the lines slightly deeper. This might be enough to result in significant changes in the correlations.

After investigating the correlations between the SD and the a-v correlation coefficients we proceed to analyze the standard deviation of the same values.

## 3.3. Standard Deviation

In this step we will calculate the standard deviation of the SD and the a-v correlation coefficients for all spaxels to see how the values vary in each of the galaxies. A high standard deviation would indicate that the values are more variable across the galaxy and vice versa. We plot the resulting standard deviations in Figure 3.3.

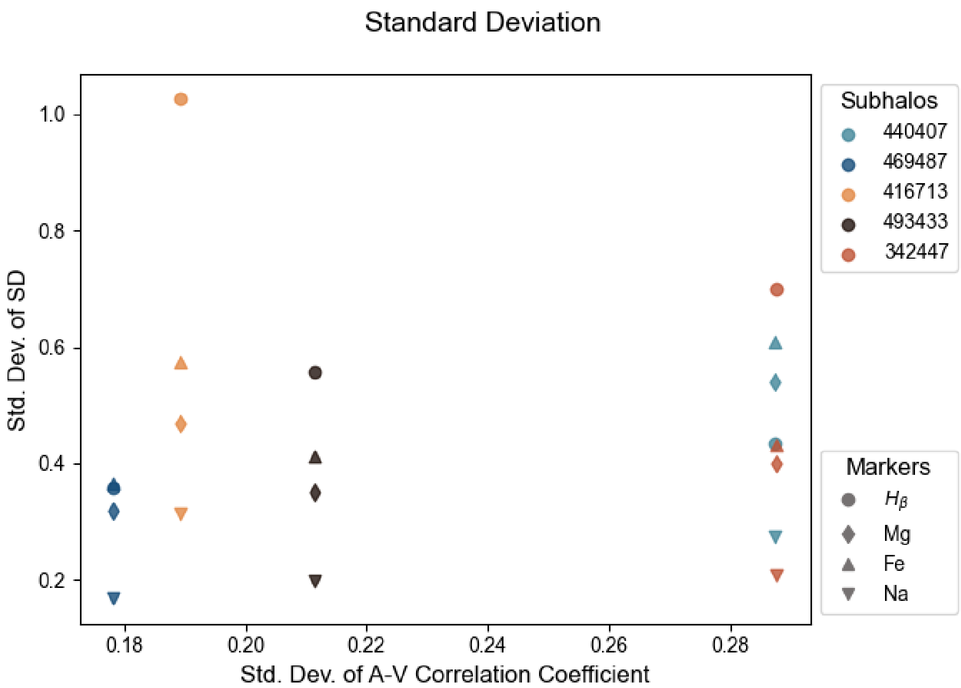


Figure 3.3.: Standard deviation of SD vs. standard deviation of a-v correlation coefficient for the whole galaxy sample. The data sets are at a 90 degree angle and we calculate the values for four different wavelength intervals.

First, we take a look at the standard deviation of the a-v correlation coefficient. Among the galaxies with one dominant component, the bulge-dominated galaxy 416713 has the lowest standard deviation, the thick disk galaxy 493433 lies in the middle, and the highest standard deviation is observed for the thin disk galaxy 342447. This indicates that the galaxies with younger stars have a higher standard deviation of the a-v correlation coefficient.

From Figure 3.3, we can also see that the standard deviations for the two galaxies with evenly spaced components lie at opposite ends. This suggests that galaxy 469487 is dynamically cold compared to galaxy 440407, which explains the different results in the correlation coefficients shown in Table 3.1.

If we look at the standard deviation of the SD we see that the $H_\beta$ interval results in the highest values and galaxy 469487 again has the lowest values.

Unfortunately our small dataset does not show a trend which could be used to predict `pPXF` residuals, but it would be interesting to create this plot with a bigger dataset. In the next Figure (3.4), we want to see what the standard deviation looks like at different angles.

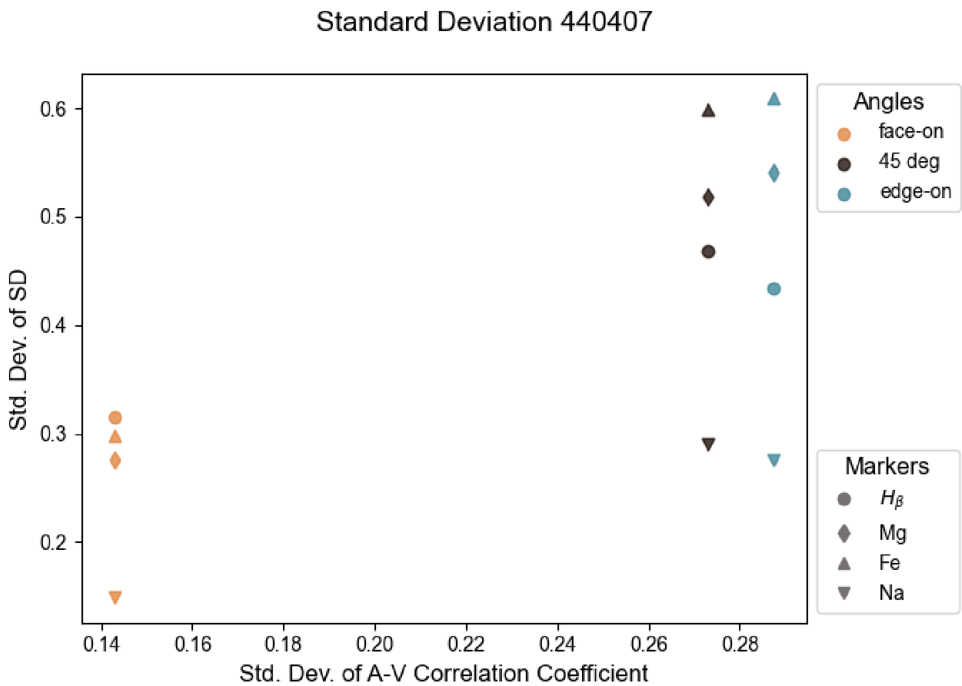


Figure 3.4.: Standard deviation of SD vs. standard deviation of a-v correlation coefficient for galaxy 440407 at three inclinations and for four different wavelength intervals.

From Figure 3.4, we can clearly see that the higher the angle, the higher the standard deviation. If we look at a galaxy edge-on, it results in more variation because there are more ages and velocities within one spaxel, whereas face-on, the range of ages and velocities is smaller within a single spaxel.

Since `pPXF` fits the data as closely to the true values as possible, the residuals expected from using the assumption 1.5 are not produced by the fitting process in the same way as in the calculated data cube. We have analyzed the correlations and standard deviations in our sample to identify potential trends, but given the small number of galaxies analyzed, the data is not sufficient to confirm any clear patterns.

# 4. Discussion

In this section, we address the key questions that guided the work presented in this thesis.

## 4.1. Which Metric Should We Use?

We intended to define a metric which accentuates the differences between the spectra of a PK-dependent and a PK-independent data cube. It should be easy to calculate and should not require a lot of computational capacity. In section 2.3 we described the three metrics we specified: The Absolute Difference (AD), the Signed Difference (SD) and the Gradient Signed Difference (GSD). Each of these metrics can depict the differences between spectra, but only the SD and the GSD can distinguish between redshift and blueshift.

We tested if our metrics correlate with the a-v correlation coefficients of the truth data cube in section 2.3.4 and found that overall, the SD has the highest correlation coefficients. The GSD has similarly high correlaction coefficients and is slightly more complicated to calculate, because it follows the gradient of the whole continuum instead of just the main absorption line like the SD.

To obtain a detectable signal with a signal to noise ratio (S/N) of 100, we need to get values of at least 1 %. Both metrics satisfy this condition with maximum values around 4.5 % for the SD compared to maximum values around 2.5 % for the GSD.

Even though the GSD seemed to be the more accurate metric, we chose the SD for this work, because it results in the highest correlation coefficients and is easier to calculate.

## 4.2. What Is The Best Line To Look At?

The best absorption line to compare the truth and the PK-independent datacube is found to be $H_\beta$, simply because it shows the highest difference values. As seen in Table 3.1 and Figure 2.10, the other lines ($Mg$, $Fe$ and $Na$) produce higher correlation coefficients between the a-v correlation coefficients and the SD, which would make them better candidates. However, the corresponding SD values rarely exceed the 1 % to make them measurable with a S/N of 100.

As shown in Figure 2.11, the young stars are responsible for the strong signal in hbeta. This aligns with the expectation that when we look at single spaxels in which young and old stellar populations are mixed together, a fit with the single-component model in pPXF would necessarily lead to more inaccuracies. Furthermore, the result is consistent with the trend of the $H_\beta$ strength decreasing with increasing $\sigma$, as discussed in Kuntschner et al. [2001].

## 4.3. How Does The Signal Change With Inclination Value?

Similar to how galaxies appear brighter if they are observed edge-on, the signal of the residuals in our data is strongest when analyzing the data from an edge-on perspective. In a visual observation this is due to the fact that more light sources are placed behind each other along the line of sight. In our case there are more data points with different ages and velocites along the line of sight which are flattened to a 2D spacial grid.

We presented this effect in Figure 3.4, where it is shown that the standard deviation of the a-v correlation coefficient is lowest for the face-on data and highest for the edge-on data. If we make the same plot for the bulge dominated galaxy we see that the a-v correlation coefficient does not change significantly with different angles. Generally the signal is highest if the data is analyzed at a 90 degree or edge-on angle.

## 4.4. Can We Find The Signal In Residuals Of PPXF Fits?

If we compare the Signed Difference of the PK-independent data cube in Figure 2.7 and of the pPXF fit in Figure 3.1, we see that the values of the SD in the pPXF fit version are smaller. Although we get some maximum SD values in the pPXF fit version that are close to the maximum SD values of the PK-independent version, the values are overall not as strong as expected and likely indistinguishable from noise in actual observations.

Although we found differences between the truth data cube and the pPXF fits, they do not follow any systematic pattern which would allow to extract any applicable information. It seems that pPXF gets very close to the true spectra by fitting every spaxel independently and exhibits a flexible fitting behavior.

## 4.5. Robustness of Results

We adjusted the pPXF parameters to obtain the best possible fit, using the truth data cube as a reference. We found that the pPXF parameters $v$ and $\sigma$ had the most effect on the quality of the fit, whereas changing the number of moments and the fitting tolerance as well as changing the resolutions of the underlying truth data cubes did not cause significant changes in the resulting fits. We obtained the fit closest to the truth by varying $v$ and $\sigma$ for every spaxel and choosing the best values. Even though comparing the fit to the initial data can't be done when using observation data, we had to assume the best possible fit, to test if our method leads to measurable residuals in any use case.

Applying the same data conversion process and `pPXF` fitting parameters to each galaxy in our sample lead to consistent and comparable outcomes, allowing for a reliable analysis across the dataset.

## 4.6. Limitations and Outlook

Since the TNG50 simulation data used in this work is free of noise, repeating the same analysis with realistic noise would maybe provide more insight. Real observation data would also contain inaccuracies due to the instruments used and environmental conditions. Therefore the effects found by our method could potentially be smaller when applied to actual IFU data.

As our approach is based solely on the MILES SSP models, and given the method's strong dependence on the underlying SSPs, it would be interesting to investigate how the choice of SSP library affects the results.

Although no clear trend is observed in the standard deviations across our current sample of five galaxies with varying component ratios, a larger sample might reveal such a relationship. Exploring this in future work should therefore be considered.

In this work we only used single-component fitting methods. Multi-component fitting methods are typically applied when velocity components are clearly separated in the signal, but in our case, the components overlap. While we have not explored multi-component fitting in this work, methods specifically designed to handle overlapping velocity components could offer a great improvement for this process in general.

Since a 1 % deviation would be detectable in observational data with $S/N = 100$ and we don't don't get interpretable results from `pPXF` residuals, it may be worth exploring other methods better suited to extract information from the residuals of single-component fitting methods, which use the assumption 1.5.

# 5. Conclusions

In this thesis, we investigated the effect of the simplification made by single-component fitting methods, namely the asusumption that locally, kinematics and populations are independent. We compared PK-dependent and PK-independent data cubes created from simulation data, analyzed the residuals from data cubes fitted with `pPXF`, investigated the influence of data quality and viewing angle and examined whether the residuals reveal trends linked to galaxy properties.

We developed three metrics to highlight differences between PK-dependent and PK-independent spectra: Absolute Difference (AD), Signed Difference (SD), and Gradient Signed Difference (GSD). While all are able to show spectral differences, we selected the Signed Difference (SD) as it provided the highest correlations with the truth data cube.

Among the absorption lines examined, $H_\beta$ is the most sensitive tracer of the differences between the truth and the PK-independent data cubes. We showed that the strong signal in $H_\beta$ is caused by young stellar populations mixed together with older stellar populations. For the same reason, the viewing angle plays an important role when it comes to the strength of the signal. Edge-on orientation of the galaxy data increases the residual signal, which reflects the diversity of stellar populations projected along the line of sight.

Despite using the simplifying assumption 1.5, the single-component `pPXF` fits produced data cubes of reasonably high quality, with residuals being smaller than expected based on the results of the PK-independent cubes created with `popkinmocks`. This indicates that `pPXF`'s approach of spaxel-by-spaxel fitting is flexible enough to reproduce the original spectra with high accuracy. Nonetheless our findings suggest, that it would be beneficial to use multi-component fitting methods, especially when there is evidence of young stellar populations.

Even though it is possible to find measurable residuals using data cubes obtained with `pPXF`, we could not extract applicable information from these residuals because every galaxy behaves differently. However, this finding may be limited by the size of our galaxy sample.

# Bibliography

P. A. R. Ade, N. Aghanim, M. Arnaud, M. Ashdown, J. Aumont, C. Baccigalupi, A. J. Banday, R. B. Barreiro, J. G. Bartlett, N. Bartolo, E. Battaner, R. Battye, K. Benabed, A. Benoît, A. Benoit-Lévy, J.-P. Bernard, M. Bersanelli, P. Bielewicz, J. J. Bock, A. Bonaldi, L. Bonavera, J. R. Bond, J. Borrill, F. R. Bouchet, F. Boulanger, M. Bucher, C. Burigana, R. C. Butler, E. Calabrese, J.-F. Cardoso, A. Catalano, A. Challinor, A. Chamballu, R.-R. Chary, H. C. Chiang, J. Chluba, P. R. Christensen, S. Church, D. L. Clements, S. Colombi, L. P. L. Colombo, C. Combet, A. Coulais, B. P. Crill, A. Curto, F. Cuttaia, L. Danese, R. D. Davies, R. J. Davis, P. de Bernardis, A. de Rosa, G. de Zotti, J. Delabrouille, F.-X. Désert, E. Di Valentino, C. Dickinson, J. M. Diego, K. Dolag, H. Dole, S. Donzelli, O. Doré, M. Douspis, A. Ducout, J. Dunkley, X. Dupac, G. Efstathiou, F. Elsner, T. A. Enßlin, H. K. Eriksen, M. Farhang, J. Fergusson, F. Finelli, O. Forni, M. Frailis, A. A. Fraisse, E. Franceschi, A. Frejsel, S. Galeotta, S. Galli, K. Ganga, C. Gauthier, M. Gerbino, T. Ghosh, M. Giard, Y. Giraud-Héraud, E. Giusarma, E. Gjerløw, J. González-Nuevo, K. M. Górski, S. Gratton, A. Gregorio, A. Gruppuso, J. E. Gudmundsson, J. Hamann, F. K. Hansen, D. Hanson, D. L. Harrison, G. Helou, S. Henrot-Versillé, C. Hernández-Monteagudo, D. Herranz, S. R. Hildebrandt, E. Hivon, M. Hobson, W. A. Holmes, A. Hornstrup, W. Hovest, Z. Huang, K. M. Huffenberger, G. Hurier, A. H. Jaffe, T. R. Jaffe, W. C. Jones, M. Juvela, E. Keihänen, R. Keskitalo, T. S. Kisner, R. Kneissl, J. Knoche, L. Knox, M. Kunz, H. Kurki-Suonio, G. Lagache, A. Lähteenmäki, J.-M. Lamarre, A. Lasenby, M. Lattanzi, C. R. Lawrence, J. P. Leahy, R. Leonardi, J. Lesgourgues, F. Levrier, A. Lewis, M. Liguori, P. B. Lilje, M. Linden-Vørnle, M. López-Caniego, P. M. Lubin, J. F. Macías-Pérez, G. Maggio, D. Maino, N. Mandolesi, A. Mangilli, A. Marchini, M. Maris, P. G. Martin, M. Martinelli, E. Martínez-González, S. Masi, S. Matarrese, P. McGehee, P. R. Meinhold, A. Melchiorri, J.-B. Melin, L. Mendes, A. Mennella, M. Migliaccio, M. Millea, S. Mitra, M.-A. Miville-Deschênes, A. Moneti, L. Montier, G. Morgante, D. Mortlock, A. Moss, D. Munshi, J. A. Murphy, P. Naselsky, F. Nati, P. Natoli, C. B. Netterfield, H. U. Nørgaard-Nielsen, F. Noviello, D. Novikov, I. Novikov, C. A. Oxborrow, F. Paci, L. Pagano, F. Pajot, R. Paladini, D. Paoletti, B. Partridge, F. Pasian, G. Patanchon, T. J. Pearson, O. Perdereau, L. Perotto, F. Perrotta, V. Pettorino, F. Piacentini, M. Piat, E. Pierpaoli, D. Pietrobon, S. Plaszczynski, E. Pointecouteau, G. Polenta, L. Popa, G. W. Pratt, G. Prézeau, S. Prunet, J.-L. Puget, J. P. Rachen, W. T. Reach, R. Rebolo, M. Reinecke, M. Remazeilles, C. Renault, A. Renzi, I. Ristorcelli, G. Rocha, C. Rosset, M. Rossetti, G. Roudier, B. Rouillé d'Orfeuil, M. Rowan-Robinson, J. A. Rubiño Martín, B. Rusholme, N. Said, V. Salvatelli, L. Salvati, M. Sandri, D. Santos, M. Savelainen, G. Savini, D. Scott, M. D. Seiffert, P. Serra, E. P. S. Shellard, L. D.

Spencer, M. Spinelli, V. Stolyarov, R. Stompor, R. Sudiwala, R. Sunyaev, D. Sutton, A.-S. Suur-Uski, J.-F. Sygnet, J. A. Tauber, L. Terenzi, L. Toffolatti, M. Tomasi, M. Tristram, T. Trombetti, M. Tucci, J. Tuovinen, M. Türler, G. Umana, L. Valenziano, J. Valiviita, F. Van Tent, P. Vielva, F. Villa, L. A. Wade, B. D. Wandelt, I. K. Wehus, M. White, S. D. M. White, A. Wilkinson, D. Yvon, A. Zacchei, and A. Zonca. Planck2015 results: Xiii. cosmological parameters. *Astronomy & Astrophysics*, 594: A13, Sept. 2016. ISSN 1432-0746. doi: 10.1051/0004-6361/201525830. URL `https://doi.org/10.1051/0004-6361/201525830`.

J. T. Allen, S. M. Croom, I. S. Konstantopoulos, J. J. Bryant, R. Sharp, G. N. Cecil, L. M. R. Fogarty, C. Foster, A. W. Green, I. T. Ho, M. S. Owers, A. L. Schaefer, N. Scott, A. E. Bauer, I. Baldry, L. A. Barnes, J. Bland-Hawthorn, J. V. Bloom, S. Brough, M. Colless, L. Cortese, W. J. Couch, M. J. Drinkwater, S. P. Driver, M. Goodwin, M. L. P. Gunawardhana, E. J. Hampton, A. M. Hopkins, L. J. Kewley, J. S. Lawrence, S. G. Leon-Saval, J. Liske, Á. R. López-Sánchez, N. P. F. Lorente, R. McElroy, A. M. Medling, J. Mould, P. Norberg, Q. A. Parker, C. Power, M. B. Pracy, S. N. Richards, A. S. G. Robotham, S. M. Sweet, E. N. Taylor, A. D. Thomas, C. Tonini, and C. J. Walcher. The sami galaxy survey: Early data release. *Monthly Notices of the Royal Astronomical Society*, 446(2):1567–1583, jan 2015. doi: 10.1093/mnras/stu2057. URL `https://doi.org/10.1093/mnras/stu2057`.

Astropy Collaboration, T. P. Robitaille, E. J. Tollerud, P. Greenfield, M. Droettboom, E. Bray, T. Aldcroft, M. Davis, A. Ginsburg, A. M. Price-Whelan, W. E. Kerzendorf, A. Conley, N. Crighton, K. Barbary, D. Muna, H. Ferguson, F. Grollier, M. M. Parikh, P. H. Nair, H. M. Unther, C. Deil, J. Woillez, S. Conseil, R. Kramer, J. E. H. Turner, L. Singer, R. Fox, B. A. Weaver, V. Zabalza, Z. I. Edwards, K. Azalee Bostroem, D. J. Burke, A. R. Casey, S. M. Crawford, N. Dencheva, J. Ely, T. Jenness, K. Labrie, P. L. Lim, F. Pierfederici, A. Pontzen, A. Ptak, B. Refsdal, M. Servillat, and O. Streicher. Astropy: A community Python package for astronomy. *Astronomy & Astrophysics*, 558:A33, Oct. 2013. doi: 10.1051/0004-6361/201322068. URL `https://doi.org/10.1051/0004-6361/201322068`.

Astropy Collaboration, A. M. Price-Whelan, B. M. Sipőcz, H. M. Günther, P. L. Lim, S. M. Crawford, S. Conseil, D. L. Shupe, M. W. Craig, N. Dencheva, A. Ginsburg, J. T. Vand erPlas, L. D. Bradley, D. Pérez-Suárez, M. de Val-Borro, T. L. Aldcroft, K. L. Cruz, T. P. Robitaille, E. J. Tollerud, C. Ardelean, T. Babej, Y. P. Bach, M. Bachetti, A. V. Bakanov, S. P. Bamford, G. Barentsen, P. Barmby, A. Baumbach, K. L. Berry, F. Biscani, M. Boquien, K. A. Bostroem, L. G. Bouma, G. B. Brammer, E. M. Bray, H. Breytenbach, H. Buddelmeijer, D. J. Burke, G. Calderone, J. L. Cano Rodríguez, M. Cara, J. V. M. Cardoso, S. Cheedella, Y. Copin, L. Corrales, D. Crichton, D. D'Avella, C. Deil, É. Depagne, J. P. Dietrich, A. Donath, M. Droettboom, N. Earl, T. Erben, S. Fabbro, L. A. Ferreira, T. Finethy, R. T. Fox, L. H. Garrison, S. L. J. Gibbons, D. A. Goldstein, R. Gommers, J. P. Greco, P. Greenfield, A. M. Groener, F. Grollier, A. Hagen, P. Hirst, D. Homeier, A. J. Horton, G. Hosseinzadeh, L. Hu, J. S. Hunkeler, Ž. Ivezić, A. Jain, T. Jenness, G. Kanarek, S. Kendrew, N. S. Kern, W. E.

Kerzendorf, A. Khvalko, J. King, D. Kirkby, A. M. Kulkarni, A. Kumar, A. Lee, D. Lenz, S. P. Littlefair, Z. Ma, D. M. Macleod, M. Mastropietro, C. McCully, S. Montagnac, B. M. Morris, M. Mueller, S. J. Mumford, D. Muna, N. A. Murphy, S. Nelson, G. H. Nguyen, J. P. Ninan, M. Nöthe, S. Ogaz, S. Oh, J. K. Parejko, N. Parley, S. Pascual, R. Patil, A. A. Patil, A. L. Plunkett, J. X. Prochaska, T. Rastogi, V. Reddy Janga, J. Sabater, P. Sakurikar, M. Seifert, L. E. Sherbert, H. Sherwood-Taylor, A. Y. Shih, J. Sick, M. T. Silbiger, S. Singanamalla, L. P. Singer, P. H. Sladen, K. A. Sooley, S. Sornarajah, O. Streicher, P. Teuben, S. W. Thomas, G. R. Tremblay, J. E. H. Turner, V. Terrón, M. H. van Kerkwijk, A. de la Vega, L. L. Watkins, B. A. Weaver, J. B. Whitmore, J. Woillez, V. Zabalza, and Astropy Contributors. The Astropy Project: Building an Open-science Project and Status of the v2.0 Core Package. *The Astronomical Journal*, 156(3):123, Sept. 2018. doi: 10.3847/1538-3881/aabc4f. URL `https://doi.org/10.3847/1538-3881/aabc4f`.

Astropy Collaboration, A. M. Price-Whelan, P. L. Lim, N. Earl, N. Starkman, L. Bradley, D. L. Shupe, A. A. Patil, L. Corrales, C. E. Brasseur, M. N"othe, A. Donath, E. Tollerud, B. M. Morris, A. Ginsburg, E. Vaher, B. A. Weaver, J. Tocknell, W. Jamieson, M. H. van Kerkwijk, T. P. Robitaille, B. Merry, M. Bachetti, H. M. G"unther, T. L. Aldcroft, J. A. Alvarado-Montes, A. M. Archibald, A. B'odi, S. Bapat, G. Barentsen, J. Baz'an, M. Biswas, M. Boquien, D. J. Burke, D. Cara, M. Cara, K. E. Conroy, S. Conseil, M. W. Craig, R. M. Cross, K. L. Cruz, F. D'Eugenio, N. Dencheva, H. A. R. Devillepoix, J. P. Dietrich, A. D. Eigenbrot, T. Erben, L. Ferreira, D. Foreman-Mackey, R. Fox, N. Freij, S. Garg, R. Geda, L. Glattly, Y. Gondhalekar, K. D. Gordon, D. Grant, P. Greenfield, A. M. Groener, S. Guest, S. Gurovich, R. Handberg, A. Hart, Z. Hatfield-Dodds, D. Homeier, G. Hosseinzadeh, T. Jenness, C. K. Jones, P. Joseph, J. B. Kalmbach, E. Karamehmetoglu, M. Kaluszy'nski, M. S. P. Kelley, N. Kern, W. E. Kerzendorf, E. W. Koch, S. Kulumani, A. Lee, C. Ly, Z. Ma, C. MacBride, J. M. Maljaars, D. Muna, N. A. Murphy, H. Norman, R. O'Steen, K. A. Oman, C. Pacifici, S. Pascual, J. Pascual-Granado, R. R. Patil, G. I. Perren, T. E. Pickering, T. Rastogi, B. R. Roulston, D. F. Ryan, E. S. Rykoff, J. Sabater, P. Sakurikar, J. Salgado, A. Sanghi, N. Saunders, V. Savchenko, L. Schwardt, M. Seifert-Eckert, A. Y. Shih, A. S. Jain, G. Shukla, J. Sick, C. Simpson, S. Singanamalla, L. P. Singer, J. Singhal, M. Sinha, B. M. SipHocz, L. R. Spitler, D. Stansby, O. Streicher, J. Šumak, J. D. Swinbank, D. S. Taranu, N. Tewary, G. R. Tremblay, M. d. Val-Borro, S. J. Van Kooten, Z. Vasovi'c, S. Verma, J. V. de Miranda Cardoso, P. K. G. Williams, T. J. Wilson, B. Winkel, W. M. Wood-Vasey, R. Xue, P. Yoachim, C. Zhang, A. Zonca, and Astropy Project Contributors. The Astropy Project: Sustaining and Growing a Community-oriented Open-source Project and the Latest Major Release (v5.0) of the Core Package. *The Astrophysical Journal*, 935(2):167, Aug. 2022. doi: 10.3847/1538-4357/ac7c74. URL `https://doi.org/10.3847/1538-4357/ac7c74`.

R. Bacon, G. Adam, A. Baranne, G. Courtes, D. Dubet, J. P. Dubois, E. Emsellem, P. Ferruit, Y. Georgelin, G. Monnet, E. Pecontal, A. Rousset, and F. Say. 3d spectrography at high spatial resolution. i. concept and realization of the integral field spectrograph tiger. *Astronomy and Astrophysics Supplement Series*, 113:347, Oct. 1995. URL `https://ui.adsabs.harvard.edu/abs/1995A%26AS..113..347B`. Provided by the SAO/NASA Astrophysics Data System.

R. Bacon, S. Conseil, D. Mary, J. Brinchmann, M. Shepherd, M. Akhlaghi, P. M. Weilbacher, L. Piqueras, L. Wisotzki, D. Lagattuta, B. Epinat, A. Guerou, H. Inami, S. Cantalupo, J. B. Courbot, T. Contini, J. Richard, M. Maseda, R. Bouwens, N. Bouché, W. Kollatschny, J. Schaye, R. A. Marino, R. Pello, C. Herenz, B. Guiderdoni, and M. Carollo. The MUSE Hubble Ultra Deep Field Survey. I. Survey description, data reduction, and source detection. *Astronomy & Astrophysics*, 608:A1, Dec. 2017. doi: 10.1051/0004-6361/201730833. URL `https://doi.org/10.1051/0004-6361/201730833`.

A. Bressan, P. Marigo, L. Girardi, B. Salasnich, C. Dal Cero, S. Rubele, and A. Nanni. Parsec: Stellar tracks and isochrones with the padova and trieste stellar evolution code. *Monthly Notices of the Royal Astronomical Society*, 427(1):127–145, Nov 2012. doi: 10.1111/j.1365-2966.2012.21948.x. URL `https://doi.org/10.1111/j.1365-2966.2012.21948.x`.

K. Bundy, M. A. Bershady, D. R. Law, R. Yan, N. Drory, N. MacDonald, D. A. Wake, B. Cherinka, J. R. Sánchez-Gallego, A.-M. Weijmans, D. Thomas, C. Tremonti, K. Masters, L. Coccato, A. M. Diamond-Stanic, A. Aragón-Salamanca, V. Avila-Reese, C. Badenes, J. Falcón-Barroso, F. Belfiore, D. Bizyaev, G. A. Blanc, J. Bland-Hawthorn, M. R. Blanton, J. R. Brownstein, N. Byler, M. Cappellari, C. Conroy, A. A. Dutton, E. Emsellem, J. Etherington, P. M. Frinchaboy, H. Fu, J. E. Gunn, P. Harding, E. J. Johnston, G. Kauffmann, K. Kinemuchi, M. A. Klaene, J. H. Knapen, A. Leauthaud, C. Li, L. Lin, R. Maiolino, V. Malanushenko, E. Malanushenko, S. Mao, C. Maraston, R. M. McDermid, M. R. Merrifield, R. C. Nichol, D. Oravetz, K. Pan, J. K. Parejko, S. F. Sanchez, D. Schlegel, A. Simmons, O. Steele, M. Steinmetz, K. Thanjavur, B. A. Thompson, J. L. Tinker, R. C. E. van den Bosch, K. B. Westfall, D. Wilkinson, S. Wright, T. Xiao, and K. Zhang. Overview of the SDSS-IV MaNGA Survey: Mapping nearby Galaxies at Apache Point Observatory. *The Astrophysical Journal*, 798(1):7, Jan. 2015. doi: 10.1088/0004-637X/798/1/7. URL `https://doi.org/10.1088/0004-637X/798/1/7`.

M. Cappellari. Improving the full spectrum fitting method: accurate convolution with Gauss-Hermite functions. *Monthly Notices of the Royal Astronomical Society*, 466(1): 798–811, Apr. 2017. doi: 10.1093/mnras/stw3020. URL `https://doi.org/10.1093/mnras/stw3020`.

M. Cappellari. Full spectrum fitting with photometry in PPXF: stellar population versus dynamical masses, non-parametric star formation history and metallicity for 3200 LEGA-C galaxies at redshift $z \approx 0.8$. *MNRAS*, 526:3273–3300, 2023. doi: 10.1093/mnras/stad2597. URL `https://doi.org/10.1093/mnras/stad2597`.

G. Chabrier. Galactic stellar and substellar initial mass function. *Publications of the*

*Astronomical Society of the Pacific*, 115(809):763–795, July 2003. doi: 10.1086/376392. URL https://doi.org/10.1086/376392. Provided by the SAO/NASA Astrophysics Data System.

S. Comerón, H. Salo, J. H. Knapen, and R. F. Peletier. The kinematics of local thick discs do not support an accretion origin. *Astronomy & Astrophysics*, 623:A89, 2019. doi: 10.1051/0004-6361/201833653. URL https://doi.org/10.1051/0004-6361/201833653.

P. T. de Zeeuw, M. Bureau, E. Emsellem, R. Bacon, C. M. Carollo, Y. Copin, R. L. Davies, H. Kuntschner, B. W. Miller, G. Monnet, R. F. Peletier, and E. K. Verolme. The SAURON project - II. Sample and early results. *Monthly Notices of the Royal Astronomical Society*, 329(3):513–530, Jan. 2002. doi: 10.1046/j.1365-8711.2002.05059.x. URL https://doi.org/10.1046/j.1365-8711.2002.05059.x.

A. Dotter, B. Chaboyer, D. Jevremović, V. Kostov, E. Baron, and J. W. Ferguson. The dartmouth stellar evolution database. *The Astrophysical Journal Supplement Series*, 178(1):89, Sep 2008. doi: 10.1086/589654. URL https://doi.org/10.1086/589654.

R. M. González Delgado, C. Leitherer, and T. M. Heckman. Synthetic spectra of h balmer and he i absorption lines. ii. evolutionary synthesis models for starburst and poststarburst galaxies. *The Astrophysical Journal Supplement Series*, 125(2):489, dec 1999. doi: 10.1086/313285. URL https://dx.doi.org/10.1086/313285.

F. Hinterer, S. Hubmer, P. Jethwa, K. M. Soodhalter, G. van de Ven, and R. Ramlau. A projected nesterov-kaczmarz approach to stellar population-kinematic distribution reconstruction in extragalactic archaeology, 2022. URL https://arxiv.org/abs/2206.03925.

P. Jethwa. popkinmocks: mock ifu datacubes for modelling stellar populations and kinematics. *Journal of Open Source Software*, 8(85):5225, 2023. doi: 10.21105/joss.05225. URL https://doi.org/10.21105/joss.05225.

M. Koleva, P. Prugniel, A. Bouchard, and Y. Wu. Ulyss: a full spectrum fitting package. *Astronomy & Astrophysics*, 501(3):1269–1279, 2009. doi: 10.1051/0004-6361/200811467. URL https://doi.org/10.1051/0004-6361/200811467.

P. Kroupa. On the variation of the initial mass function. *Monthly Notices of the Royal Astronomical Society*, 322(2):231–246, April 2001. doi: 10.1046/j.1365-8711.2001.04022.x. URL https://doi.org/10.1046/j.1365-8711.2001.04022.x. Provided by the SAO/NASA Astrophysics Data System.

H. Kuntschner, J. R. Lucey, R. J. Smith, M. J. Hudson, and R. L. Davies. On the dependence of spectroscopic indices of early-type galaxies on age, metallicity and velocity dispersion. *Monthly Notices of the Royal Astronomical Society*, 323(3):615–629, May 2001. ISSN 1365-2966. doi: 10.1046/j.1365-8711.2001.04263.x. URL https://doi.org/10.1046/j.1365-8711.2001.04263.x.

F. Marinacci, M. Vogelsberger, R. Pakmor, P. Torrey, V. Springel, L. Hernquist, D. Nelson, R. Weinberger, A. Pillepich, J. Naiman, and S. Genel. First results from the IllustrisTNG simulations: radio haloes and magnetic fields. *Monthly Notices of the Royal Astronomical Society*, 480(4):5113–5139, 08 2018. ISSN 0035-8711. doi: 10.1093/mnras/sty2206. URL `https://doi.org/10.1093/mnras/sty2206`.

H. Mo, F. C. van den Bosch, and S. White. *Galaxy Formation and Evolution*. Cambridge University Press, 2010. doi: 10.1017/CBO9780511807244. URL `https://doi.org/10.1017/CBO9780511807244`.

J. P. Naiman, A. Pillepich, V. Springel, E. Ramirez-Ruiz, P. Torrey, M. Vogelsberger, R. Pakmor, D. Nelson, F. Marinacci, L. Hernquist, R. Weinberger, and S. Genel. First results from the IllustrisTNG simulations: a tale of two elements - chemical evolution of magnesium and europium. *Monthly Notices of the Royal Astronomical Society*, 477(1):1206–1224, 03 2018. ISSN 0035-8711. doi: 10.1093/mnras/sty618. URL `https://doi.org/10.1093/mnras/sty618`.

D. Nelson, A. Pillepich, V. Springel, R. Weinberger, L. Hernquist, R. Pakmor, S. Genel, P. Torrey, M. Vogelsberger, G. Kauffmann, F. Marinacci, and J. Naiman. First results from the IllustrisTNG simulations: the galaxy colour bimodality. *Monthly Notices of the Royal Astronomical Society*, 475(1):624–647, 11 2017. ISSN 0035-8711. doi: 10.1093/mnras/stx3040. URL `https://doi.org/10.1093/mnras/stx3040`.

D. Nelson, A. Pillepich, V. Springel, R. Pakmor, R. Weinberger, S. Genel, P. Torrey, M. Vogelsberger, F. Marinacci, and L. Hernquist. First results from the TNG50 simulation: galactic outflows driven by supernovae and black hole feedback. *Monthly Notices of the Royal Astronomical Society*, 490(3):3234–3261, Dec. 2019. doi: 10.1093/mnras/stz2306. URL `https://doi.org/10.1093/mnras/stz2306`.

A. Pillepich, D. Nelson, L. Hernquist, V. Springel, R. Pakmor, P. Torrey, R. Weinberger, S. Genel, J. P. Naiman, F. Marinacci, and M. Vogelsberger. First results from the IllustrisTNG simulations: the stellar mass content of groups and clusters of galaxies. *Monthly Notices of the Royal Astronomical Society*, 475(1):648–675, 12 2017a. ISSN 0035-8711. doi: 10.1093/mnras/stx3112. URL `https://doi.org/10.1093/mnras/stx3112`.

A. Pillepich, V. Springel, D. Nelson, S. Genel, J. Naiman, R. Pakmor, L. Hernquist, P. Torrey, M. Vogelsberger, R. Weinberger, and F. Marinacci. Simulating galaxy formation with the illustristng model. *Monthly Notices of the Royal Astronomical Society*, 473(3):4077–4106, Oct. 2017b. ISSN 1365-2966. doi: 10.1093/mnras/stx2656. URL `https://doi.org/10.1093/mnras/stx2656`.

A. Pillepich, D. Nelson, V. Springel, R. Pakmor, P. Torrey, R. Weinberger, M. Vogelsberger, F. Marinacci, S. Genel, A. van der Wel, and L. Hernquist. First results from the TNG50 simulation: the evolution of stellar and gaseous discs across cosmic time. *Monthly Notices of the Royal Astronomical Society*, 490(3):3196–3233, Dec. 2019. doi: 10.1093/mnras/stz2338. URL `https://doi.org/10.1093/mnras/stz2338`.

A. Pillepich, D. Sotillo-Ramos, R. Ramesh, D. Nelson, C. Engler, V. Rodriguez-Gomez, M. Fournier, M. Donnari, V. Springel, and L. Hernquist. Milky way and andromeda analogues from the tng50 simulation. *Monthly Notices of the Royal Astronomical Society*, 535(2):1721–1762, 09 2024. ISSN 0035-8711. doi: 10.1093/mnras/stae2165. URL `https://doi.org/10.1093/mnras/stae2165`.

F. F. Rosales-Ortega, R. C. Kennicutt, S. F. Sánchez, A. I. Díaz, A. Pasquali, B. D. Johnson, and C. N. Hao. Pings: the ppak ifs nearby galaxies survey. *Monthly Notices of the Royal Astronomical Society*, 405(2):735–758, June 2010. doi: 10.1111/j.1365-2966.2010.16498.x. URL `https://doi.org/10.1111/j.1365-2966.2010.16498.x`.

E. E. Salpeter. The luminosity function and stellar evolution. *The Astrophysical Journal*, 121:161, Jan 1955. doi: 10.1086/145971. URL `https://doi.org/10.1086/145971`. Provided by the SAO/NASA Astrophysics Data System.

S. F. Sánchez, R. C. Kennicutt, A. Gil de Paz, G. van de Ven, J. M. Vílchez, L. Wisotzki, C. J. Walcher, D. Mast, J. A. L. Aguerri, S. Albiol-Pérez, A. Alonso-Herrero, J. Alves, J. Bakos, T. Bartáková, J. Bland-Hawthorn, A. Boselli, D. J. Bomans, A. Castillo-Morales, C. Cortijo-Ferrero, A. de Lorenzo-Cáceres, A. Del Olmo, R. J. Dettmar, A. Díaz, S. Ellis, J. Falcón-Barroso, H. Flores, A. Gallazzi, B. García-Lorenzo, R. González Delgado, N. Gruel, T. Haines, C. Hao, B. Husemann, J. Iglésias-Páramo, K. Jahnke, B. Johnson, B. Jungwiert, V. Kalinova, C. Kehrig, D. Kupko, Á. R. López-Sánchez, M. Lyubenova, R. A. Marino, E. Mármol-Queraltó, I. Márquez, J. Masegosa, S. Meidt, J. Mendez-Abreu, A. Monreal-Ibero, C. Montijo, A. M. Mourão, G. Palacios-Navarro, P. Papaderos, A. Pasquali, R. Peletier, E. Pérez, I. Pérez, A. Quirrenbach, M. Relaño, F. F. Rosales-Ortega, M. M. Roth, T. Ruiz-Lara, P. Sánchez-Blázquez, C. Sengupta, R. Singh, V. Stanishev, S. C. Trager, A. Vazdekis, K. Viironen, V. Wild, S. Zibetti, and B. Ziegler. CALIFA, the Calar Alto Legacy Integral Field Area survey. I. Survey presentation. *Astronomy & Astrophysics*, 538:A8, Feb. 2012. doi: 10.1051/0004-6361/201117353. URL `https://doi.org/10.1051/0004-6361/201117353`.

P. Sanchez-Blazquez, R. F. Peletier, J. Jimenez-Vicente, N. Cardiel, A. J. Cenarro, J. Falcon-Barroso, J. Gorgas, S. Selam, and A. Vazdekis. Medium-resolution isaac newton telescope library of empirical spectra. *Monthly Notices of the Royal Astronomical Society*, 371(2):703–718, Sept. 2006. ISSN 1365-2966. doi: 10.1111/j.1365-2966.2006.10699.x. URL `https://doi.org/10.1111/j.1365-2966.2006.10699.x`.

M. Sarzi, E. Iodice, and T. F. Collaboration. The fornax3d survey - a magnitude-limited study of galaxies in the fornax cluster with muse. *The Messenger vol. 189*, 189:9–14, Dec. 2022. doi: 10.18727/0722-6691/5284. URL `https://doi.org/10.18727/0722-6691/5284`.

S. Sharma, M. R. Hayden, J. Bland-Hawthorn, D. Stello, S. Buder, J. C. Zinn, T. Kallinger, M. Asplund, G. M. De Silva, V. D'Orazi, K. Freeman, J. Kos, G. F. Lewis, J. Lin, K. Lind, S. Martell, J. D. Simpson, R. A. Wittenmyer, D. B. Zucker, T. Zwitter, B. Chen, K. Cotar, J. Esdaile, M. Hon, J. Horner, D. Huber, P. R. Kafle, S. Khanna, Y.-S. Ting, D. M. Nataf, T. Nordlander, M. H. M. Saadon, T. Tepper-Garcia, C. G. Tinney, G. Traven, F. Watson, D. Wright, and R. F. G. Wyse. Fundamental relations for the velocity dispersion of stars in the milky way. *Monthly Notices of the Royal Astronomical Society*, 506(2):1761–1776, jun 2021. doi: 10.1093/mnras/stab1086. URL `https://doi.org/10.1093/mnras/stab1086`.

Soubiran, C., Bienaymé, O., Mishenina, T. V., and Kovtyukh, V. V. Vertical distribution of galactic disk stars - iv. amr and avr from clump giants. *A&A*, 480(1):91–101, 2008. doi: 10.1051/0004-6361:20078788. URL `https://doi.org/10.1051/0004-6361:20078788`.

V. Springel, R. Pakmor, A. Pillepich, R. Weinberger, D. Nelson, L. Hernquist, M. Vogelsberger, S. Genel, P. Torrey, F. Marinacci, and J. Naiman. First results from the IllustrisTNG simulations: matter and galaxy clustering. *Monthly Notices of the Royal Astronomical Society*, 475(1):676–698, 12 2017. ISSN 0035-8711. doi: 10.1093/mnras/stx3304. URL `https://doi.org/10.1093/mnras/stx3304`.

J. van de Sande, A. Fraser-McKelvie, D. B. Fisher, M. Martig, M. R. Hayden, and the GECKOS Survey collaboration. The geckos survey: Turning galaxy evolution on its side with deep observations of edge-on galaxies with and without bars, July 2023. URL `https://doi.org/10.5281/zenodo.8131220`.

G. van de Ven, J. Falcón-Barroso, and M. Lyubenova. Extragalactic archaeology: The assembly history of galaxies from dynamical and stellar population models. *Annual Review of Astronomy and Astrophysics*, 63:–, May 2025. doi: 10.1146/annurev-astro-052622-025659. URL `https://doi.org/10.1146/annurev-astro-052622-025659`.

R. P. van der Marel and M. Franx. A new method for the identification of non-gaussian line profiles in elliptical galaxies. *The Astrophysical Journal*, 407:525, Apr. 1993. doi: 10.1086/172534. URL `https://doi.org/10.1086/172534`. Provided by the SAO/NASA Astrophysics Data System.

R. Weinberger, V. Springel, L. Hernquist, A. Pillepich, F. Marinacci, R. Pakmor, D. Nelson, S. Genel, M. Vogelsberger, J. Naiman, and P. Torrey. Simulating galaxy formation with black hole driven thermal and kinetic feedback. *Monthly Notices of the Royal Astronomical Society*, 465(3):3291–3308, Nov. 2016. ISSN 1365-2966. doi: 10.1093/mnras/stw2944. URL `https://doi.org/10.1093/mnras/stw2944`.

R. P. C. Wiersma, J. Schaye, T. Theuns, C. Dalla Vecchia, and L. Tornatore. Chemical enrichment in cosmological, smoothed particle hydrodynamics simulations. *Monthly Notices of the Royal Astronomical Society*, 399(2):574–600, Oct. 2009. ISSN 1365-2966. doi: 10.1111/j.1365-2966.2009.15331.x. URL `https://doi.org/10.1111/j.1365-2966.2009.15331.x`.

P. Yoachim and J. J. Dalcanton. The kinematics of thick disks in nine external galaxies. *The Astrophysical Journal*, 682(2):1004, aug 2008. doi: 10.1086/589553. URL `https://dx.doi.org/10.1086/589553`.

# A. Appendix

## A.1. Appendix A

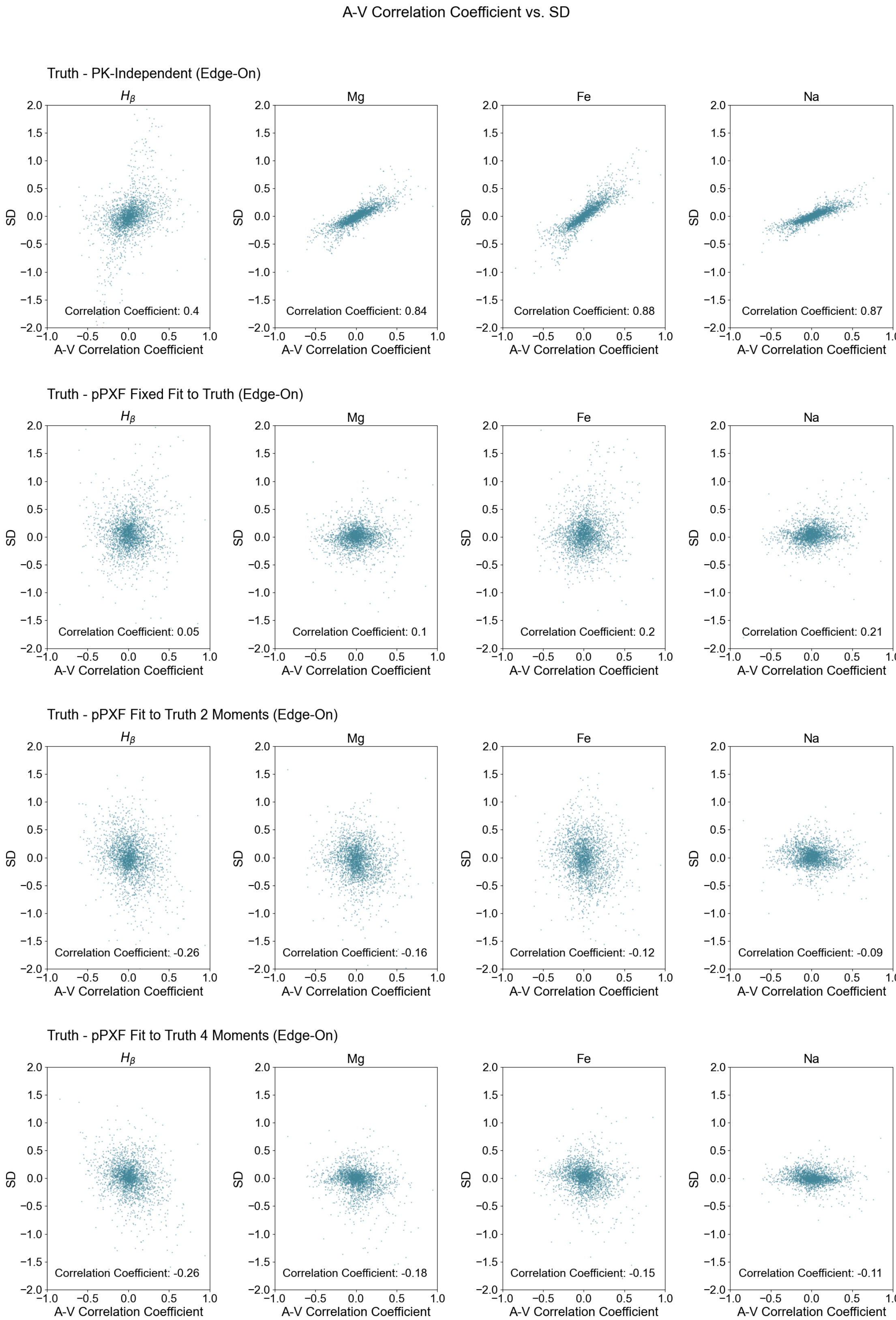


Figure A.1.: Galaxy 469487 (evenly distributed components): SD vs. a-v correlation coefficients at four different wavelength intervals and at a 90 deg angle (edge-on) for the Kin. Ind. cube and three different fitting combinations with `pPXF`.

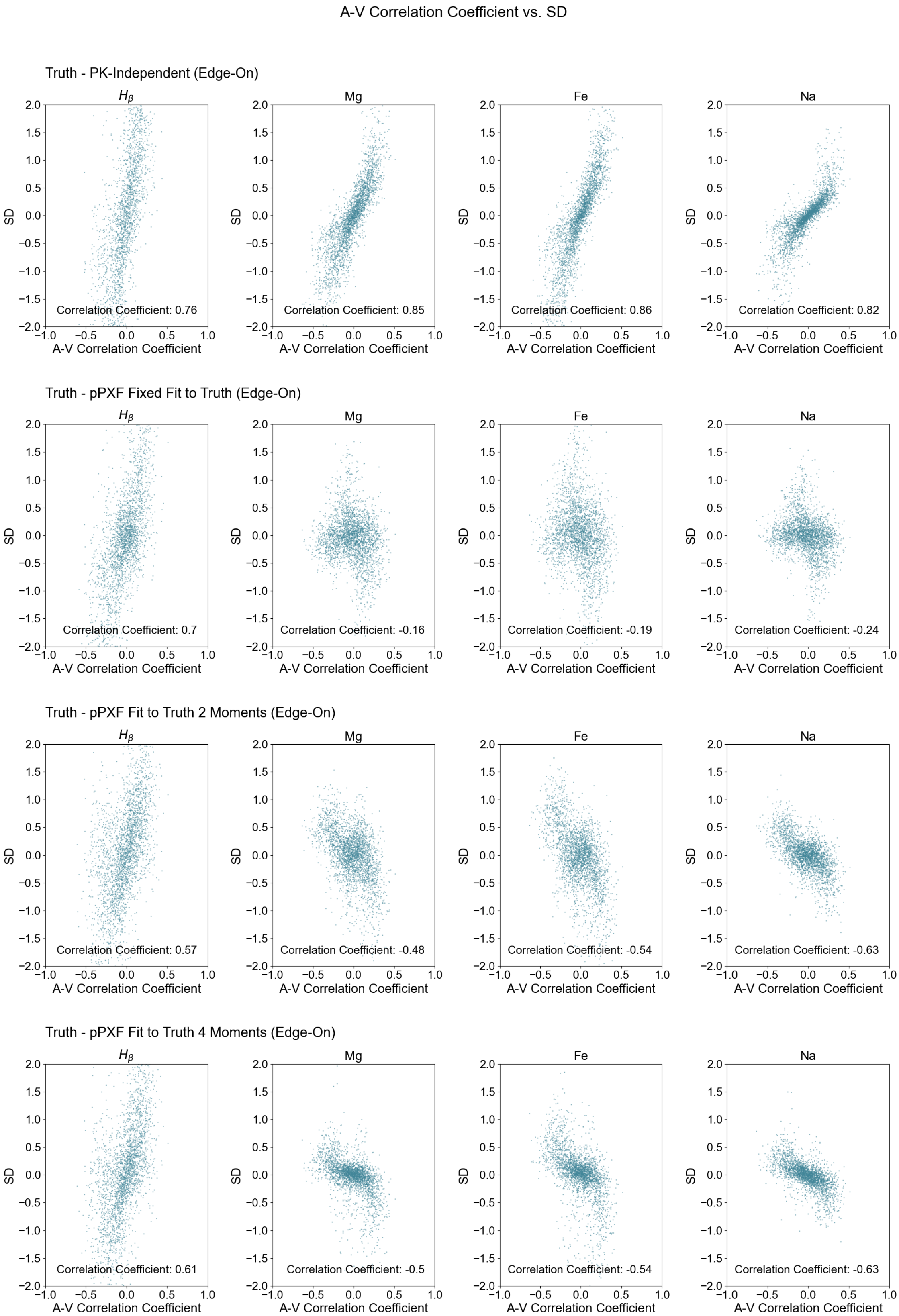


Figure A.2.: Galaxy 416713 (dominant bulge component): SD vs. a-v correlation coefficients at four different wavelength intervals and at a 90 deg angle (edge-on) for the Kin. Ind. cube and three different fitting combinations with `pPXF`.

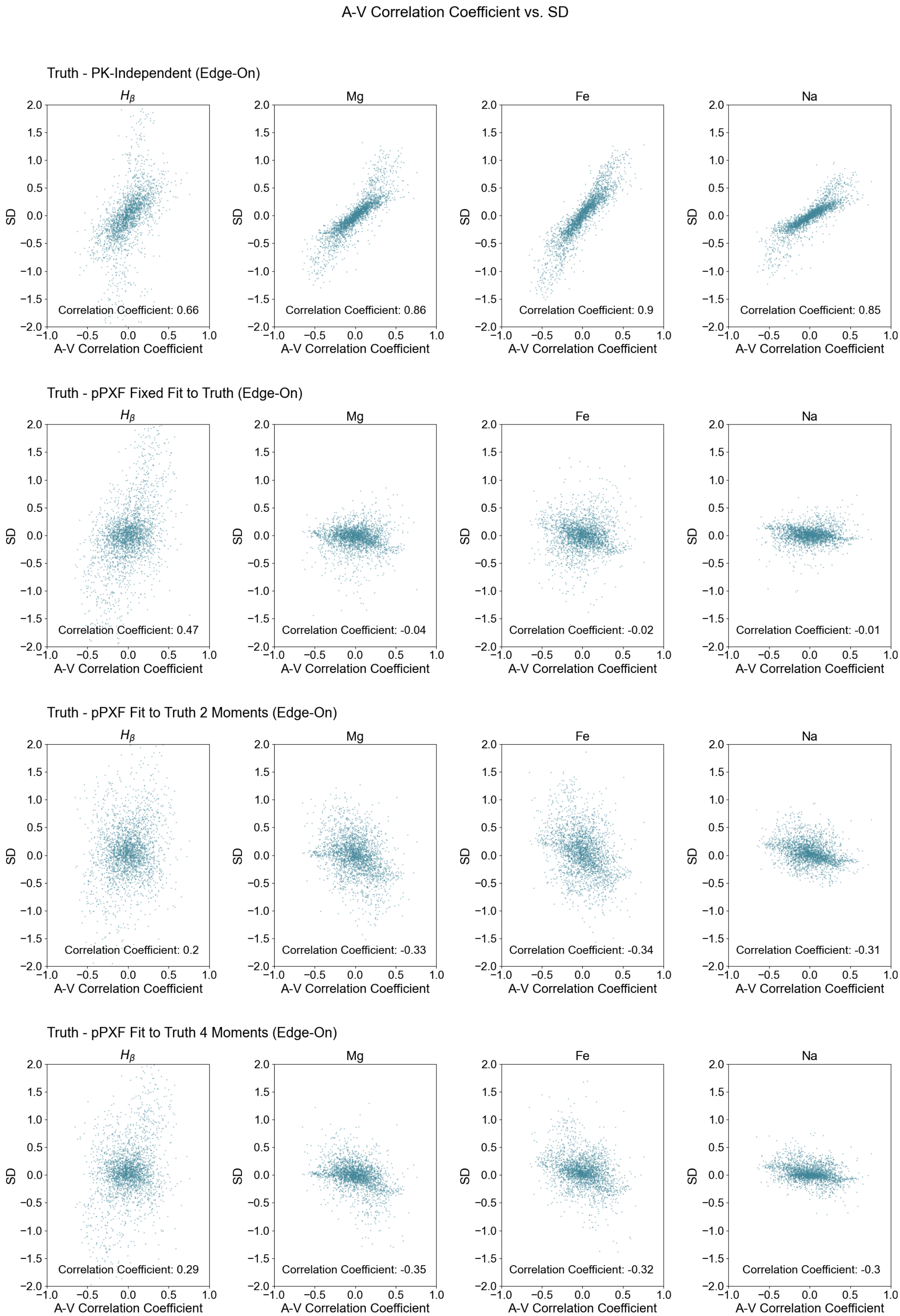


Figure A.3.: Galaxy 493433 (dominant thick disk component): SD vs. a-v correlation coefficients at four different wavelength intervals and at a 90 deg angle (edge-on) for the Kin. Ind. cube and three different fitting combinations with `pPXF`.

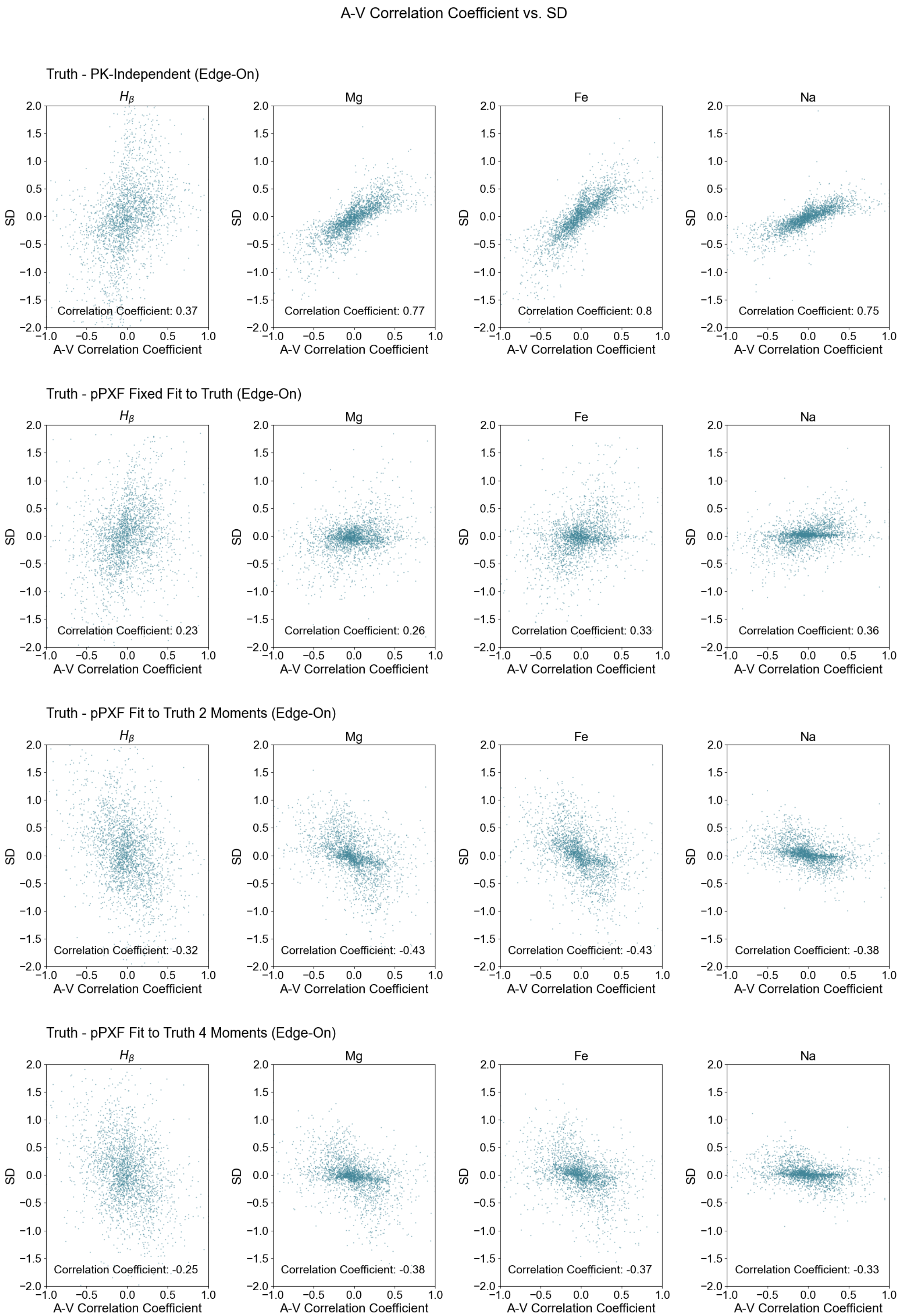


Figure A.4.: Galaxy 342447 (dominant thin disk component): SD vs. a-v correlation coefficients at four different wavelength intervals and at a 90 deg angle (edge-on) for the Kin. Ind. cube and three different fitting combinations with `pPXF`.